Generalized Chapman-Enskog continuum breakdown parameters for chemically reacting flows

Krishnan Swaminathan-Gopalan, Sharanya Subramaniam, and Kelly A. Stephani

Generalized Chapman-Enskog Continuum Breakdown Parameters for Chemically Reacting Flows

Krishnan Swaminathan-Gopalan,* Sharanya Subramaniam,* and Kelly A. Stephani[†]

Department of Mechanical Science and Engineering
University of Illinois at Urbana-Champaign
(Dated: November 2, 2016)

The Generalized Chapman-Enskog (GCE) method for rapid and slow thermo-chemical processes is employed to formulate a set of continuum breakdown parameters for chemically reacting flows. These GCE breakdown parameters are derived for one-temperature, two-temperature and three-temperature models, through classification of the relevant thermo-chemical timescales relative to fast elastic collisional processes and slow flow processes associated with changes in macroscopic observables. Continuum breakdown mechanisms owing to multi-component diffusion, thermal diffusion, normal and shear stresses, Fourier-type heat fluxes based on translational, rotational and vibrational temperatures, bulk viscosity and relaxation pressure are presented for chemically reacting flows. The GCE breakdown parameters, derived from rigorous kinetic theory capture the proper physical mechanism leading to continuum breakdown. These breakdown parameters are then used to analyze continuum breakdown in a Mach 24 reacting air flow over a sphere, and continuum breakdown was observed in the shock, and close to the sphere surface. The flow field near the sphere surface was found to be characterized by sharp species concentration gradients due to gas-phase and surface reactions. Chemical reactions thus lead indirectly to the distortion of the VDF, providing a new pathway to continuum breakdown which is captured by the GCE species-wise diffusion breakdown parameter.

---

* Ph.D. candidate, Department of Mechanical Science and Engineering.
† Assistant Professor, Department of Mechanical Science and Engineering; Corresponding author: ksteph@illinois.edu

I. INTRODUCTION

Multiscale flows involving mixed regions of continuum and rarefied flow regimes are common in a variety of engineering applications, from microelectromechanical system (MEMS) devices to high-speed atmospheric entry vehicles. Simulation techniques developed for multiscale flow modeling require an accurate description of rarefaction effects, which are most suitably captured by kinetic solvers, such as direct methods for the Boltzmann equation or particle based methods like direct simulation Monte Carlo (DSMC) [1]. While kinetic methods may be employed from continuum to free molecular flow regimes, they are most commonly used for modeling non-equilibrium flows characterized by Knudsen number $Kn \geqslant 0.1$. Approaching the continuum limit, the flow field may be accurately modeled with continuum (Euler or Navier-Stokes) solvers, which provide a computationally efficient alternative to the kinetic solvers, but these solutions become inaccurate outside of the hydrodynamic regime. It is precisely in this regime, however, that a high-fidelity kinetic solver may be employed. Thus, a combined continuum/kinetic approach is often adopted as a way to achieve high-fidelity solutions across a broad range of flow regimes, while maintaining computational efficiency.

Hybrid multiscale methods have been developed and successfully applied to a wide range of flow problems [2–6]. These combined approaches typically involve spatial coupling of computational fluid dynamics (CFD) solvers, based on Euler or Navier-Stokes continuum descriptions, with kinetic solvers, based on BGK, direct Boltzmann or the particle-based DSMC method. One of the key components of hybrid solvers is defining the hybrid interface as well as the interface location. The hybrid interface is a computational boundary in physical space dividing the regions of continuum and rarefied flow, and facilitates the transfer of flow field information between the continuum/kinetic solvers. To maximize computational efficiency, it is important to determine where, in physical space, the continuum solution method begins to break down, and the kinetic solution method should be employed.

The onset of continuum breakdown is characterized by a departure of the underlying velocity distribution function from its equilibrium, Maxwellian form. CFD solvers based on the Navier-Stokes equations provide accurate solutions for systems involving *small departures* from equilibrium, expressed mathematically as a perturbation of the Maxwellian distribution, or the well-known Chapman-Enskog distribution [7]. Physically, the hydrodynamic quantities of number density, velocity and temperature are 'carried' by the equilibrium Maxwellian distribution, while the perturbation of the Maxwellian distribution manifests as higher-order fluxes, including heat flux, normal and shear stresses for a simple gas. The Navier-Stokes equations incorporate these higher-order effects in the governing equations through the constitutive relationships, which provide closure for the equations and allow for the relation of internal stresses and heat fluxes to gradients of the macroscopic observables. Provided that the departure from equilibrium is small, the constitutive relations hold and the Navier-Stokes equations are valid.

When flow field gradients become large or characteristic length scales become comparable to the molecular mean free path, the underlying velocity distribution function exhibits strong departure from equilibrium, and can no longer be mathematically expressed as a small perturbation by Chapman-Enskog theory. Under these conditions, the closure of the Navier-Stokes equations through the constitutive relations is no longer valid, and a kinetic description is necessary.

II. CONTINUUM BREAKDOWN PARAMETERS

Continuum breakdown parameters are dimensionless quantities that are used to characterize the degree of departure from an equilibrium Maxwellian distribution and to determine when continuum breakdown has occurred. These quantities are generally compared against a continuum breakdown criterion, which relates the magnitude of the breakdown parameter for a given physical mechanism (e.g., entropy generation rate, gradients in density, velocity, temperature, etc.) to a measure of non-equilibrium [8–10]. The breakdown criterion is selected as a threshold below which macroscopic observables from both continuum and kinetic solutions are in good agreement, generally within 5% [9, 11–13]. Although a number of different approaches to identify continuum breakdown have been proposed, this work focuses on continuum breakdown parameters as determined by expressions involving macroscopic quantities obtained from a CFD (Navier-Stokes) solution. Furthermore, this work adopts the breakdown criteria values established in previous investigations to facilitate comparisons with the new breakdown parameters and discussions herein.

Bird [8] had proposed a continuum breakdown parameter for steady and unsteady expanding flows. For steady, expanding flows the parameter takes the form,

$$P = \frac{\sqrt{\pi}}{2} s \frac{\lambda}{\rho} \left| \frac{d\rho}{dl} \right| \tag{1}$$

The quantities, ρ and λ are the local density and mean free path respectively, s - the speed ratio - is given by $s = u\beta$, where u is the local velocity and β is the inverse most probable speed and l represents the distance along a streamline.

In a later work, Bird [14] put forth the concept of a local Knudsen number based on the length scale of macroscopic gradients, for assessing the validity of the continuum approximation for a given flow system. This concept was furthered by Boyd [9, 15] to form the Gradient-Length-Local (GLL) Knudsen number, which is one of the most widely used parameters for assessing continuum breakdown for compressing/expanding hypersonic flows based on a Navier-Stokes solution. This parameter is expressed as the ratio of the local mean free path and a length scale determined by flow gradients:

$$Kn_{GLL} = \frac{\lambda}{Q_{local}} \left| \frac{dQ}{dx} \right|, \tag{2}$$

where λ is the local mean free path, Q is a macroscopic observable such as density, velocity magnitude or temperature, whose gradients are calculated with respect to a flow field distance. When Q is set as the velocity magnitude, $Q_{local} = max(|\boldsymbol{v}|, a)$ where a is the local sonic speed [16].

A more rigorous formulation of the continuum breakdown parameters for *steady flows* may be obtained directly from the Chapman-Enskog method, involving expansion of the velocity distribution function $f(\boldsymbol{C})$ in a small parameter, which provides the governing equations for systems which exhibit *small departures* from equilibrium. To first order in the Chapman-Enskog expansion, the distribution function $f(\boldsymbol{C})$ is expressed as the equilibrium (Maxwellian) distribution function $f^{(0)}(\boldsymbol{C})$ plus a perturbation:

$$f(\boldsymbol{C}) = f^{(0)}(\boldsymbol{C}) \left(1 + \phi^{(1)}(\boldsymbol{C}) \right), \tag{3}$$

where $\phi^{(1)}(\boldsymbol{C})$ is the first-order Chapman-Enskog perturbation on $f^{(0)}(\boldsymbol{C})$. Upon substitution of Eq. 3 into the Boltzmann equation, a general form for the perturbation $\phi^{(1)}(\boldsymbol{C})$ for a simple (single-species, mono-atomic) gas is obtained [7, 17]:

$$\phi^{(1)}(\boldsymbol{C}) = -\frac{1}{n}\mathbf{A}(\boldsymbol{C}) \cdot \nabla \log T - \frac{1}{n}\mathbf{B}(\boldsymbol{C}) : \nabla v, \tag{4}$$

where $\mathbf{A}(\boldsymbol{C})$ and $\mathbf{B}(\boldsymbol{C})$ are vector and tensor functions of the thermal velocity, $\boldsymbol{C}$. These functions appear in the definitions for the transport coefficients of viscosity, μ and thermal conductivity, k_{tr} as bracket integrals:

$$\mu = \frac{1}{10} k_B T [\mathbf{B}, \mathbf{B}], \tag{5}$$

$$k_{tr} = \frac{1}{3} k_B [\mathbf{A}, \mathbf{A}]. \tag{6}$$

The solution of the unknown functions $\mathbf{A}$ and $\mathbf{B}$ is typically approximated through expansion in Sonine polynomials (an exact solution may be obtained exclusively for the case of Maxwell molecules), and explicit expressions for the transport coefficients are thus obtained to first order in Sonine polynomials in terms of the Ω-integrals:

$$\mu = \frac{5k_B T}{8\Omega^{(2,2)}} \tag{7}$$

$$k_{tr} = \frac{25c_{v,tr}k_B T}{16\Omega^{(2,2)}} \tag{8}$$

Upon substitution into Eq. 4, the expression for $\phi^{(1)}$ becomes:

$$\phi^{(1)}(\boldsymbol{C}) = (q_x \mathcal{C}_x + q_y \mathcal{C}_y + q_z \mathcal{C}_z) \left(\frac{2}{5}\mathcal{C}^2 - 1 \right)$$

$$-2 \left(\mathcal{C}_x \mathcal{C}_y \tau_{xy} + \mathcal{C}_x \mathcal{C}_z \tau_{xz} + \mathcal{C}_y \mathcal{C}_z \tau_{yz} \right) \tag{9}$$

$$- \left(\mathcal{C}_x^2 \tau_{xx} + \mathcal{C}_y^2 \tau_{yy} + \mathcal{C}_z^2 \tau_{zz} \right) \tag{10}$$

where the quantities τ_{ij} and q_i are dimensionless quantities defined as:

$$\tau_{ij} = \frac{\mu}{p}\left(\partial_j v_i + \partial_i v_j - \frac{2}{3}\partial_k v_k \delta_{ij}\right) \tag{11}$$

$$q_i = -\frac{2\beta}{p}k_{tr}\partial_i T \tag{12}$$

These dimensionless quantities, presented by Garcia and Alder [13], are the Chapman-Enskog continuum breakdown parameters for a simple (single-species, mono-atomic) gas, and appear as the coefficients of the terms on the right-hand side of Eq. 9. The perturbation in this case is only a function of thermal velocity normalized by the most probable thermal speed, $\mathcal{C}_i = C_i/\sqrt{2k_b T/m}$. Large values for Eq. 11 and Eq. 12 indicate that the departure from equilibrium may no longer be considered as a small perturbation, and the Navier-Stokes equations are no longer valid.

The use of such breakdown parameters for problems involving high-temperature aerothermodynamics requires the assessment of continuum breakdown for gas mixtures with excited internal energy states and chemical reactions. Deschenes et al. [11, 12] presented an extension of the Gradient-Length-Local Knudsen number for continuum breakdown due to rotational non-equilibrium. Other high-temperature continuum breakdown mechanisms such as vibrational non-equilibrium and chemical reactions were not considered, owing to the idea that such processes occur over characteristic time scales much greater than the elastic collisional time scale. This effort formally addresses this assumption using the Generalized Chapman-Enskog method from kinetic theory.

The Generalized Chapman-Enskog (GCE) method introduces a formal approach for deriving the continuum breakdown parameters for problems involving fast and slow high-temperature thermochemical processes [18]. This formalism allows for the continuum breakdown parameters to be determined precisely and in a way that is consistent with the underlying governing equations employed in the CFD solver. The Generalized Chapman-Enkog method was first employed by Stephani et al. [19] to derive a new set of continuum breakdown parameters for chemically frozen flows. This formulation recovers the same continuum breakdown parameters by Garcia and Alder [13], but includes additional breakdown parameters for non-equilibrium characterized by diffusion fluxes and internal (rotational and vibrational) heat fluxes.

The aim of this work is to present a complete set of Generalized Chapman-Enskog continuum breakdown parameters for chemically reacting, steady flows. The method for rapid and slow thermochemical processes outlined by Nagnibeda and Kustova [18] is applied for one temperature, two-temperature and three-temperature models, and the corresponding sets of breakdown parameters are presented for each (Section III). The GCE parameters are then applied to evaluate continuum breakdown in a Mach 24 reacting air flow over a sphere, and the role of chemical reactions as an indirect mechanism for continuum breakdown is assessed (Section IV). A detailed comparison of the GCE and GLL breakdown parameter mathematical forms (Section III E) and breakdown mechanisms (Section IV D) in the reacting flow study is made, and conclusions are presented in Section V.

III. FORMULATION OF GCE BREAKDOWN PARAMETERS

A. Method for Rapid and Slow processes

In high speed, high-temperature flows where non-equilibrium thermal and chemical processes become important, the relaxation time scales of various collisional processes (elastic and inelastic) can vary substantially. In general, relaxation times for elastic and inelastic processes relative to the characteristic time of variation of macroscopic quantities are:

$$\tau_{el} \lesssim \tau_{rot} \ll \tau_{vib} < \tau_{react} \sim \theta \tag{13}$$

where characteristic times are τ_{el} for elastic collisions, τ_{rot} and τ_{vib} for collisions with rotational and vibrational exchange, and τ_{react} for reactions (inelastic collisions), and θ is the characteristic time of change in macroscopic quantities. This effectively divides collisional processes into two groups: rapid processes with time scales much smaller than θ ($\tau_{rap} \ll \theta$) and slow processes with time scales on the order of θ ($\tau_{sl} \sim \theta$).

This variability in time scales is introduced in the Generalized Chapman-Enskog analysis through definition of the small parameter $\varepsilon = \tau/\theta$. In consideration of rapid and slow processes the kinetic equation can be written as:

$$\frac{\partial f}{\partial t} + \boldsymbol{c} \cdot \nabla_{\boldsymbol{x}} f = \frac{1}{\varepsilon} J^{rap} + J^{sl} \tag{14}$$

Using this approach, the collision operator is separated into two parts, J^{rap} weighted by $1/\varepsilon = \theta/\tau_{rap} \gg 1$, and J^{sl} weighted by $1/\varepsilon = \theta/\tau_{sl} \sim \mathbf{O}(1)$. The Generalized Chapman-Enskog method is then used as before to express the distribution function to first order as:

$$f = f^{(0)} + \varepsilon f^{(1)} = f^{(0)} \left(1 + \phi_{GCE}\right) \tag{15}$$

The aim of this work is to find the GCE breakdown parameters as determined by casting ϕ_{GCE} in terms of known Navier-Stokes flux quantities. In the following sections, three different approximations are imposed on the relative time scales introduced in Eq. 13, namely one-temperature, two-temperature and three-temperature assumptions, to construct the appropriate set of continuum breakdown parameters for use with each of these models employed in a continuum solver.

B.   One-temperature Model

In the one-temperature model, the translational and internal modes are assumed to be in equilibrium with each other and are represented by a single temperature. The associated characteristic relaxation time scales are expressed as:

$$\tau_{T-T} < \tau_{R-R} \lesssim \tau_{V-V} < \tau_{T-R-V} \ll \tau_{react} \sim \theta, \tag{16}$$

where $\tau_{T-T}, \tau_{R-R}, \tau_{V-V}$ are the characteristic time scales for the energy exchange within each mode, and τ_{T-R-V} is the time scale for the inter-modal energy exchange. In the one-temperature approximation, the energy exchange between the translational and internal energy modes are rapid processes, while the chemical reactions are on the order of the gas dynamic time scales and treated as slow processes:

$$\begin{aligned} J^{rap} &= J^{T-T} + J^{R-R} + J^{V-V} + J^{T-R-V}, \\ J^{sl} &= J^{react}. \end{aligned} \tag{17}$$

Under the one-temperature approximation, the Generalized Chapman-Enskog perturbation $\phi_{GCE,s}$ for species s is of the form [18]:

$$\phi_{GCE,s} = -\frac{1}{n}\mathbf{A}_s \cdot \nabla ln(T_{tr}) - \frac{1}{n}\sum_t \mathbf{D}_s^t \cdot \boldsymbol{d}_t - \frac{1}{n}\mathbf{B}_s : \nabla\mathbf{v} - \frac{1}{n}\mathrm{F}_s \nabla \cdot \mathbf{v} - \frac{1}{n}\mathrm{G}_s. \tag{18}$$

The generalized functions $\mathbf{A}_s$ & $\mathbf{D}_s^t$ are vector functions of the reduced peculiar velocity $\boldsymbol{\mathcal{C}}_s$, while $\mathbf{B}_s$ is a tensor function of $\boldsymbol{\mathcal{C}}_s$ and F_s & G_s are scalars. The second term on the right side of Eq. 18 contains the term $\boldsymbol{d}_t$, which is the diffusion driving force for species t defined as:

$$\boldsymbol{d}_t = \nabla\left(\frac{n_t}{n}\right) + \left(\frac{n_t}{n} - \frac{\rho_t}{\rho}\right)\nabla ln(p). \tag{19}$$

The solutions of the unknown generalized functions are obtained as expansions in the Sonine ($\mathcal{S}_\nu^n(x)$) and Waldmann-Trübenbacher ($\mathcal{P}^n(x)$) polynomials with accompanying expansion coefficients (e.g., $a_{s,rpq}$):

$$\mathbf{A}_s = -\left(\frac{m_s}{2k_bT_{tr}}\right)^{1/2} \boldsymbol{\mathcal{C}}_s \sum_{rpq} a_{s,rpq}\mathcal{S}_{3/2}^{(r)}\left(\mathcal{C}_s^2\right)\mathcal{P}^{(p)}(\varepsilon_{rot,s})\mathcal{P}^{(q)}(\varepsilon_{vib,s}),$$

$$\mathbf{D}_s^t = \left(\frac{m_s}{2k_bT_{tr}}\right)^{1/2} \boldsymbol{\mathcal{C}}_s \sum_r d_{s,r}^t\mathcal{S}_{3/2}^{(r)}\left(\mathcal{C}_s^2\right),$$

$$\mathbf{B}_s = \left(\boldsymbol{\mathcal{C}}_s\boldsymbol{\mathcal{C}}_s - \frac{1}{3}\mathcal{C}_s^2\mathbb{I}\right)\sum_r b_{s,r}\mathcal{S}_{3/2}^{(r)}\left(\mathcal{C}_s^2\right), \tag{20}$$

$$\mathrm{F}_s = \sum_{rpq} f_{s,rpq}\mathcal{S}_{1/2}^{(r)}\left(\mathcal{C}_s^2\right)\mathcal{P}^{(p)}(\varepsilon_{rot,s})\mathcal{P}^{(q)}(\varepsilon_{vib,s}),$$

$$\mathrm{G}_s = -\sum_{rpq} g_{s,rpq}\mathcal{S}_{1/2}^{(r)}\left(\mathcal{C}_s^2\right)\mathcal{P}^{(p)}(\varepsilon_{rot,s})\mathcal{P}^{(q)}(\varepsilon_{vib,s}).$$

Note that all functions in Eq. 20 are expanded by polynomials in the rapid processes only, which for the single-temperature approximation include $\mathcal{C}_s$, $\epsilon_{rot,s}$, and $\epsilon_{vib,s}$. The transport coefficients of thermal conductivity (translational – $k_{tr,s}$, rotational – $k_{rot,s}$, and vibrational – $k_{vib,s}$), viscosity (shear – μ_s, and bulk – ζ_s), multicomponent diffusion (mass – D_{st} and thermal – $D_{T,s}$) and relaxation pressure ($p_{rel,s}$) may be expressed in terms of the expansion coefficients [18]:

$$k_{tr,s} + k_{rot,s} + k_{vib,s} = \frac{k_b}{3}\left[\mathbf{A}_s, \mathbf{A}_s\right] \Rightarrow \begin{cases} k_{tr,s} &= \frac{5k_b}{4}\frac{n_s}{n}a_{s,100}, \\ k_{rot,s} &= \frac{m_sc_{v,rot,s}}{2}\frac{n_s}{n}a_{s,010}, \\ k_{vib,s} &= \frac{m_sc_{v,vib,s}}{2}\frac{n_s}{n}a_{s,001}, \end{cases}$$

$$D_{T,s} = \frac{1}{3n}\left[\mathbf{D}_s^t, \mathbf{A}_s\right] = -\frac{1}{2n}a_{s,000},$$

$$D_{st} = \frac{1}{3n}\left[\mathbf{D}_s^t, \mathbf{D}_s^t\right] = \frac{1}{2n}d_{s,0}^t, \tag{21}$$

$$\mu_s = \frac{k_bT_{tr}}{10}\left[\mathbf{B}_s, \mathbf{B}_s\right] = \frac{k_bT_{tr}}{2}\frac{n_s}{n}b_{s,0},$$

$$\zeta_s = k_bT_{tr}\left[\mathrm{F}_s, \mathrm{F}_s\right] = -k_bT_{tr}\frac{n_s}{n}f_{s,100},$$

$$p_{rel,s} = k_bT_{tr}\left[\mathrm{F}_s, \mathrm{G}_s\right] = k_bT_{tr}\frac{n_s}{n}g_{s,100}.$$

New transport mechanisms are considered in this work from that of Stephani *et al.* [19]. These include the thermal component of diffusion resulting from temperature gradients, bulk viscosity which arises from inelastic inter-modal (T-R-V) energy exchange (a rapid process in the single-temperature model) and the relaxation pressure, which is a result of the existence of rapid and slow inelastic processes. Chemical relaxation is the only slow process considered in this case. Substituting these transport coefficient expressions (Eq. 21) into Eq. 20, we arrive at the final expression for the generalized functions:

$$\mathbf{A}_s = \mathbf{A}_{s,T} + \mathbf{A}_{s,tr} + \mathbf{A}_{s,rot} + \mathbf{A}_{s,vib},$$

$$\mathbf{A}_{s,T} = \left(\frac{m_s}{2k_bT_{tr}}\right)^{1/2} 2nD_{T,s}\boldsymbol{\mathcal{C}}_s,$$

$$\mathbf{A}_{s,tr} = -\left(\frac{m_s}{2k_bT_{tr}}\right)^{1/2} \frac{4K_{tr,s}}{5k_b}\frac{n}{n_s}\left(\frac{5}{2} - \mathcal{C}_s^2\right)\boldsymbol{\mathcal{C}}_s,$$

$$\mathbf{A}_{s,rot} = -\left(\frac{m_s}{2k_bT_{tr}}\right)^{1/2} \frac{2K_{rot,s}}{m_sc_{v,rot,s}}\frac{n}{n_s}\left(\bar{\varepsilon}_{rot,s} - \varepsilon_{rot,s}\right)\boldsymbol{\mathcal{C}}_s,$$

$$\mathbf{A}_{s,vib} = -\left(\frac{m_s}{2k_bT_{tr}}\right)^{1/2} \frac{2K_{vib,s}}{m_sc_{v,vib,s}}\frac{n}{n_s}\left(\bar{\varepsilon}_{vib,s} - \varepsilon_{vib,s}\right)\boldsymbol{\mathcal{C}}_s, \tag{22}$$

$$\mathbf{D}_s^t = \left(\frac{m_s}{2k_bT_{tr}}\right)^{1/2} 2nD_{st}\boldsymbol{\mathcal{C}}_s,$$

$$\mathbf{B}_s = \frac{2\mu_s}{k_bT_{tr}}\frac{n}{n_s}\left(\boldsymbol{\mathcal{C}}_s\boldsymbol{\mathcal{C}}_s - \frac{1}{3}\mathcal{C}_s^2\mathbb{I}\right),$$

$$\mathrm{F}_s = -\frac{\zeta_s}{k_bT_{tr}}\frac{n}{n_s}\left(\frac{3}{2} - \mathcal{C}_s^2\right),$$

$$\mathrm{G}_s = \frac{p_{rel,s}}{k_bT_{tr}}\frac{n}{n_s}\left(\frac{3}{2} - \mathcal{C}_s^2\right).$$

The perturbation defined in Eq. 18 can now be expressed in terms of the transport coefficients:

$$\begin{aligned}
\phi_{GCE,s} = &-\frac{1}{n}\sum_t\left(\frac{m_s}{2k_bT_{tr}}\right)^{1/2} 2nD_{st}\boldsymbol{\mathcal{C}}_s \cdot \boldsymbol{d}_t - \frac{1}{n}\left(\frac{m_s}{2k_bT_{tr}}\right)^{1/2} 2nD_{T,s}\boldsymbol{\mathcal{C}}_s \cdot \nabla ln(T_{tr}) \\
&-\frac{1}{n}\left(\frac{m_s}{2k_bT_{tr}}\right)^{1/2} \frac{4K_{tr,s}}{5k_b}\frac{n}{n_s}\left(\mathcal{C}_s^2 - \frac{5}{2}\right)\boldsymbol{\mathcal{C}}_s \cdot \nabla ln(T_{tr}) \\
&-\frac{1}{n}\left(\frac{m_s}{2k_bT_{tr}}\right)^{1/2} \frac{2K_{rot,s}}{m_sc_{v,rot,s}}\frac{n}{n_s}\left(\varepsilon_{rot,s} - \bar{\varepsilon}_{rot,s}\right)\boldsymbol{\mathcal{C}}_s \cdot \nabla ln(T_{tr}) \\
&-\frac{1}{n}\left(\frac{m_s}{2k_bT_{tr}}\right)^{1/2} \frac{2K_{vib,s}}{m_sc_{v,vib,s}}\frac{n}{n_s}\left(\varepsilon_{vib,s} - \bar{\varepsilon}_{vib,s}\right)\boldsymbol{\mathcal{C}}_s \cdot \nabla ln(T_{tr}) \\
&-\frac{1}{n}\frac{2\mu_s}{k_bT_{tr}}\frac{n}{n_s}\left(\boldsymbol{\mathcal{C}}_s\boldsymbol{\mathcal{C}}_s - \frac{1}{3}\mathcal{C}_s^2\mathbb{I}\right) : \nabla\mathbf{v} \\
&-\frac{1}{n}\frac{\zeta_s}{k_bT_{tr}}\frac{n}{n_s}\left(\mathcal{C}_s^2 - \frac{3}{2}\right)\nabla \cdot \mathbf{v} + \frac{1}{n}\frac{p_{rel,s}}{k_bT_{tr}}\frac{n}{n_s}\left(\mathcal{C}_s^2 - \frac{3}{2}\right)
\end{aligned} \tag{23}$$

The diffusion fluxes in the Navier-Stokes solvers are expressed in terms of the diffusion velocity, which has contributions from mass and thermal diffusion:

$$\boldsymbol{V}_s = \boldsymbol{V}_{M,s} + \boldsymbol{V}_{T,s} = -\sum_t D_{st}\boldsymbol{d}_t - D_{T,s}\nabla ln(T_{tr}). \tag{24}$$

Using Eq. 24 and introducing the pressure $p_s = n_sk_bT_{tr}$, density $\rho_s = m_sn_s$ and inverse most probable thermal speed $\beta_s = \sqrt{m_s/2k_bT_{tr}}$, the perturbation takes the form:

$$\phi_{GCE,s} = 2\beta_s \boldsymbol{V}_{M,s} \cdot \boldsymbol{C}_s + 2\beta_s \boldsymbol{V}_{T,s} \cdot \boldsymbol{C}_s$$
$$- \frac{4\beta_s k_{tr,s}}{5 p_s} \left(\mathcal{C}_s^2 - \frac{5}{2} \right) \boldsymbol{C}_s \cdot \nabla T_{tr}$$
$$- \frac{2\beta_s k_{rot,s}}{\rho_s c_{v,rot,s} T_{tr}} \left(\varepsilon_{rot,s} - \bar{\varepsilon}_{rot,s} \right) \boldsymbol{C}_s \cdot \nabla T_{tr}$$
$$- \frac{2\beta_s k_{vib,s}}{\rho_s c_{v,vib,s} T_{tr}} \left(\varepsilon_{vib,s} - \bar{\varepsilon}_{vib,s} \right) \boldsymbol{C}_s \cdot \nabla T_{tr} \tag{25}$$
$$- \frac{2\mu_s}{p_s} \boldsymbol{C}_s \boldsymbol{C}_s : \left(\frac{1}{2} \left(\nabla \mathbf{v} + \nabla^T \mathbf{v} \right) - \frac{1}{3} \nabla \cdot \mathbf{v} \mathbb{I} \right)$$
$$- \frac{\zeta_s}{p_s} \left(\mathcal{C}_s^2 - \frac{3}{2} \right) \nabla \cdot \mathbf{v} + \frac{p_{rel,s}}{p_s} \left(\mathcal{C}_s^2 - \frac{3}{2} \right).$$

Finally, the Generalized Chapman-Enskog perturbation $\phi_{GCE,s}$ can be cast in terms of flux-based quantities that are readily available from a CFD solution:

$$\phi_{GCE,s} = \boldsymbol{D}_{M,s} \cdot \boldsymbol{C}_s + \boldsymbol{D}_{T,s} \cdot \boldsymbol{C}_s + \boldsymbol{q}_{tr,s} \cdot \boldsymbol{C}_s \left(\mathcal{C}_s^2 - \frac{5}{2} \right) + \boldsymbol{q}_{rot,s} \cdot \boldsymbol{C}_s \left(\varepsilon_{rot,s} - \bar{\varepsilon}_{rot,s} \right)$$
$$+ \boldsymbol{q}_{vib,s} \cdot \boldsymbol{C}_s \left(\varepsilon_{vib,s} - \bar{\varepsilon}_{vib,s} \right) + \boldsymbol{\tau}_s : \boldsymbol{C}_s \boldsymbol{C}_s + P_{bulk,s} \left(\mathcal{C}_s^2 - \frac{3}{2} \right) + P_{rel,s} \left(\mathcal{C}_s^2 - \frac{3}{2} \right). \tag{26}$$

The coefficients on the right-hand side of Eq. 26 are the Generalized Chapman-Enskog continuum breakdown parameters for a reacting gas mixture assuming a single-temperature model:

$$\boldsymbol{D}_{M,s} = \frac{2\beta_s \rho_s \boldsymbol{V}_{M,s}}{\rho_s} = \frac{2\beta_s \boldsymbol{D}_{M,s}^{NS}}{\rho_s},$$
$$\boldsymbol{D}_{T,s} = \frac{2\beta_s \rho_s \boldsymbol{V}_{T,s}}{\rho_s} = \frac{2\beta_s \boldsymbol{D}_{T,s}^{NS}}{\rho_s},$$
$$\boldsymbol{q}_{tr,s} = -\frac{4\beta_s}{5 p_s} k_{tr,s} \nabla T_{tr} = \frac{4\beta_s \boldsymbol{q}_{tr,s}^{NS}}{5 p_s},$$
$$\boldsymbol{q}_{rot,s} = -\frac{2\beta_s}{\rho_s c_{v,rot,s} T_{tr}} k_{rot,s} \nabla T_{tr} = \frac{2\beta_s \boldsymbol{q}_{rot,s}^{NS}}{\rho_s c_{v,rot,s} T_{tr}},$$
$$\boldsymbol{q}_{vib,s} = -\frac{2\beta_s}{\rho_s c_{v,vib,s} T_{tr}} k_{vib,s} \nabla T_{tr} = \frac{2\beta_s \boldsymbol{q}_{vib,s}^{NS}}{\rho_s c_{v,vib,s} T_{tr}}, \tag{27}$$
$$\boldsymbol{\tau}_s = \frac{2\mu_s}{p_s} \left(\frac{1}{2} \left(\nabla \mathbf{v} + \nabla^T \mathbf{v} \right) - \frac{1}{3} \nabla \cdot \mathbf{v} \mathbb{I} \right) = \frac{\boldsymbol{\tau}_s^{NS}}{p_s},$$
$$P_{bulk,s} = -\frac{1}{p_s} \zeta_s \nabla \cdot \mathbf{v} = \frac{p_{bulk,s}^{NS}}{p_s},$$
$$P_{rel,s} = \frac{p_{rel,s}^{NS}}{p_s}.$$

The GCE continuum breakdown parameters may be computed directly from the Navier-Stokes flux quantities (indicated on far right-hand side of Eq. 27 by the superscript NS) of mass diffusion, thermal diffusion, Fourier heat fluxes (translational, rotational and vibrational) based on gradients of a single temperature T_{tr}, viscous stress, bulk stress and relaxation pressure due to chemical reactions.

C. Two-temperature Model

In the two-temperature model, the translational and rotational energy modes are assumed to be in equilibrium and are represented by a single temperature T_{tr}. The vibrational energy exchange (V-V) is also assumed to be rapid,

however the energy exchange between translational/rotational and vibrational modes (TR-V) is considered as a slow process, thus resulting in a separate vibrational temperature T_{vib}. The associated characteristic relaxation time scales are expressed as:

$$\tau_{T-T} < \tau_{R-R} \lesssim \tau_{V-V} \lesssim \tau_{T-R} \ll \tau_{TR-V} < \tau_{react} \sim \theta, \tag{28}$$

and the rapid and slow collision operators for the kinetic equation corresponding to Eq. 14 are:

$$\begin{aligned} J^{rap} &= J^{T-T} + J^{R-R} + J^{T-R} + J^{V-V}, \\ J^{sl} &= J^{TR-V} + J^{react}. \end{aligned} \tag{29}$$

For a mixture of gases following the two-temperature model with the simple harmonic oscillator approximation, the Generalized Chapman-Enskog (GCE) perturbation $\phi_{GCE,s}$ is of the form [18]:

$$\phi_{GCE,s} = -\frac{1}{n}\mathbf{A}_s.\nabla ln(T_{tr}) - \frac{1}{n}\mathbf{A}_s^{(v)}.\nabla ln(T_{vib}) - \frac{1}{n}\sum_t \mathbf{D}_s^t.\mathbf{d}_t - \frac{1}{n}\mathbf{B}_s : \nabla\mathbf{v} - \frac{1}{n}\mathbf{F}_s\nabla.\mathbf{v} - \frac{1}{n}\mathbf{G}_s. \tag{30}$$

Since the TR-V exchanges are considered as slow processes, the perturbation in the two-temperature model has an additional term $\mathbf{A}_s^{(v)}$, associated with the gradients in the vibrational temperature. Additionally, only translational and rotational terms are present in $\mathbf{F}_s$ (below), which represents fast inelastic processes in the system. The definitions of the other functions in $\phi_{GCE,s}$ are the same as in Eq. 20. The Sonine and Waldmann-Trübenbacher polynomial expansion of the generalized functions are given by:

$$\begin{aligned} \mathbf{A}_s &= -\left(\frac{m_s}{2k_bT_{tr}}\right)^{1/2}\boldsymbol{\mathcal{C}}_s\sum_{rp}a_{s,rp}\mathcal{S}_{3/2}^{(r)}\left(\mathcal{C}_s^2\right)\mathcal{P}^{(p)}(\varepsilon_{rot,s}), \\ \mathbf{A}_s^{(v)} &= -\left(\frac{m_s}{2k_bT_{tr}}\right)^{1/2}\boldsymbol{\mathcal{C}}_s\sum_q a_{s,q}^{(v)}\mathcal{P}^{(q)}(\varepsilon_{vib,s}), \\ \mathbf{D}_s^t &= \left(\frac{m_s}{2k_bT_{tr}}\right)^{1/2}\boldsymbol{\mathcal{C}}_s\sum_r d_{s,r}^t\mathcal{S}_{3/2}^{(r)}\left(\mathcal{C}_s^2\right), \\ \mathbf{B}_s &= \left(\boldsymbol{\mathcal{C}}_s\boldsymbol{\mathcal{C}}_s - \frac{1}{3}\mathcal{C}_s^2\mathbb{I}\right)\sum_r b_{s,r}\mathcal{S}_{3/2}^{(r)}\left(\mathcal{C}_s^2\right), \\ \mathbf{F}_s &= \sum_{rp}f_{s,rp}\mathcal{S}_{1/2}^{(r)}\left(\mathcal{C}_s^2\right)\mathcal{P}^{(p)}(\varepsilon_{rot,s}), \\ \mathbf{G}_s &= -\sum_{rpq}g_{s,rpq}\mathcal{S}_{1/2}^{(r)}\left(\mathcal{C}_s^2\right)\mathcal{P}^{(p)}(\varepsilon_{rot,s})\mathcal{P}^{(q)}(\varepsilon_{vib,s}). \end{aligned} \tag{31}$$

The transport coefficients are next expressed in terms of the polynomial expansion coefficients [18]:

$$\begin{aligned} k_{tr,s} + k_{rot,s} &= \frac{k_b}{3}\left[\mathbf{A}_s, \mathbf{A}_s\right] \Rightarrow \begin{cases} k_{tr,s} &= \frac{5k_b}{4}\frac{n_s}{n}a_{s,10}, \\ k_{rot,s} &= \frac{m_s c_{v,rot,s}}{2}\frac{n_s}{n}a_{s,01}, \end{cases} \\ k_{vib,s} &= \frac{k_b}{3}\left[\mathbf{A}_s^{(v)}, \mathbf{A}_s^{(v)}\right] = \frac{m_s c_{v,vib,s}}{2}\frac{n_s}{n}a_{s,1}^{(v)}, \\ D_{T,s} &= \frac{1}{3n}\left[\mathbf{D}_s^t, \mathbf{A}_s\right] = -\frac{1}{2n}a_{s,00}, \\ D_{T,s}^{(v)} &= \frac{1}{3n}\left[\mathbf{D}_s^t, \mathbf{A}_s^{(v)}\right] = -\frac{1}{2n}a_{s,0}^{(v)}, \\ D_{st} &= \frac{1}{3n}\left[\mathbf{D}_s^t, \mathbf{D}_s^t\right] = \frac{1}{2n}d_{s,0}^t, \\ \mu_s &= \frac{k_bT_{tr}}{10}\left[\mathbf{B}_s, \mathbf{B}_s\right] = \frac{k_bT_{tr}}{2}\frac{n_s}{n}b_{s,0}, \\ \zeta_s &= k_bT_{tr}\left[\mathbf{F}_s, \mathbf{F}_s\right] = -k_bT_{tr}\frac{n_s}{n}f_{s,10}, \\ p_{rel,s} &= k_bT_{tr}\left[\mathbf{F}_s, \mathbf{G}_s\right] = k_bT_{tr}\frac{n_s}{n}g_{s,100}. \end{aligned} \tag{32}$$

Note that there is an additional thermal diffusion coefficient, arising from the separate vibrational temperature in the two-temperature model approximation. Using the above definitions, the first-order approximation to the generalized functions can be represented in terms of the transport coefficients:

$$
\begin{aligned}
\mathbf{A}_s &= \mathbf{A}_{s,T} + \mathbf{A}_{s,tr} + \mathbf{A}_{s,rot}, \\
\mathbf{A}_s^{(v)} &= \mathbf{A}_{s,T}^{(v)} + \mathbf{A}_{s,vib}^{(v)}, \\
\mathbf{A}_{s,T} &= \left(\frac{m_s}{2k_b T_{tr}}\right)^{1/2} 2nD_{T,s}\boldsymbol{\mathcal{C}}_s, \\
\mathbf{A}_{s,tr} &= -\left(\frac{m_s}{2k_b T_{tr}}\right)^{1/2} \frac{4k_{tr,s}}{5k_b} \frac{n}{n_s}\left(\frac{5}{2} - \mathcal{C}_s^2\right)\boldsymbol{\mathcal{C}}_s, \\
\mathbf{A}_{s,rot} &= -\left(\frac{m_s}{2k_b T_{tr}}\right)^{1/2} \frac{2k_{rot,s}}{m_s c_{v,rot,s}} \frac{n}{n_s}\left(\bar{\varepsilon}_{rot,s} - \varepsilon_{rot}\right)\boldsymbol{\mathcal{C}}_s, \\
\mathbf{A}_{s,T}^{(v)} &= \left(\frac{m_s}{2k_b T_{tr}}\right)^{1/2} 2nD_{T,s}^{(v)}\boldsymbol{\mathcal{C}}_s, \\
\mathbf{A}_{s,vib}^{(v)} &= -\left(\frac{m_s}{2k_b T_{tr}}\right)^{1/2} \frac{2k_{vib,s}}{m_s c_{v,vib,s}} \frac{n}{n_s}\left(\bar{\varepsilon}_{vib,s} - \varepsilon_{vib}\right)\boldsymbol{\mathcal{C}}_s, \\
\mathbf{D}_s^t &= \left(\frac{m_s}{2k_b T_{tr}}\right)^{1/2} 2nD_{st}\boldsymbol{\mathcal{C}}_s, \\
\mathbf{B}_s &= \frac{2\mu_s}{k_b T_{tr}} \frac{n}{n_s}\left(\boldsymbol{\mathcal{C}}_s\boldsymbol{\mathcal{C}}_s - \frac{1}{3}\mathcal{C}_s^2\mathbb{I}\right), \\
\mathbf{F}_s &= -\frac{\zeta_s}{k_b T_{tr}} \frac{n}{n_s}\left(\frac{3}{2} - \mathcal{C}_s^2\right), \\
\mathbf{G}_s &= \frac{p_{rel,s}}{k_b T_{tr}} \frac{n}{n_s}\left(\frac{3}{2} - \mathcal{C}_s^2\right).
\end{aligned}
\tag{33}
$$

The diffusion velocity is again introduced, which for the two-temperature model has an additional thermal diffusion term:

$$
\boldsymbol{V}_s = \boldsymbol{V}_{M,s} + \boldsymbol{V}_{T,s} + \boldsymbol{V}_{T,s}^{(v)} = -\sum_t D_{st}\boldsymbol{d}_t - D_{T,s}\nabla ln(T_{tr}) - D_{T,s}^{(v)}\nabla ln(T_{vib}).
\tag{34}
$$

Expressing the diffusion terms using the diffusion velocity and following a procedure similar to the one-temperature model, the perturbation becomes:

$$
\begin{aligned}
\phi_{GCE,s} = \; & 2\beta_s\boldsymbol{V}_{M,s}\cdot\boldsymbol{\mathcal{C}}_s + 2\beta_s\boldsymbol{V}_{T,s}\cdot\boldsymbol{\mathcal{C}}_s + 2\beta_s\boldsymbol{V}_{T,s}^{(v)}\cdot\boldsymbol{\mathcal{C}}_s \\
& - \frac{4\beta_s k_{tr,s}}{5p_s}\left(\mathcal{C}_s^2 - \frac{5}{2}\right)\boldsymbol{\mathcal{C}}_s\cdot\nabla T_{tr} \\
& - \frac{2\beta_s k_{rot,s}}{\rho_s c_{v,rot,s}T_{tr}}\left(\varepsilon_{rot,s} - \bar{\varepsilon}_{rot,s}\right)\boldsymbol{\mathcal{C}}_s\cdot\nabla T_{tr} \\
& - \frac{2\beta_s k_{vib,s}}{\rho_s c_{v,vib,s}T_{vib}}\left(\varepsilon_{vib,s} - \bar{\varepsilon}_{vib,s}\right)\boldsymbol{\mathcal{C}}_s\cdot\nabla T_{vib} \\
& - \frac{2\mu_s}{p_s}\boldsymbol{\mathcal{C}}_s\boldsymbol{\mathcal{C}}_s : \left(\frac{1}{2}\left(\nabla\mathbf{v} + \nabla^T\mathbf{v}\right) - \frac{1}{3}\nabla\cdot\mathbf{v}\mathbb{I}\right) \\
& - \frac{\zeta_s}{p_s}\left(\mathcal{C}_s^2 - \frac{3}{2}\right)\nabla\cdot\mathbf{v} + \frac{p_{rel,s}}{p_s}\left(\mathcal{C}_s^2 - \frac{3}{2}\right),
\end{aligned}
\tag{35}
$$

and the Generalized Chapman-Enskog perturbation $\phi_{GCE,s}$ for the two-temperature model is expressed in terms of flux-based quantities as:

$$\phi_{GCE,s} = \boldsymbol{D}_{M,s} \cdot \boldsymbol{C}_s + \boldsymbol{D}_{T,s} \cdot \boldsymbol{C}_s + \boldsymbol{D}_{T,s}^{(v)} \cdot \boldsymbol{C}_s + \boldsymbol{q}_{tr,s} \cdot \boldsymbol{C}_s \left(\mathcal{C}_s^2 - \frac{5}{2} \right) + \boldsymbol{q}_{rot,s} \cdot \boldsymbol{C}_s \left(\varepsilon_{rot,s} - \bar{\varepsilon}_{rot,s} \right)$$
$$+ \boldsymbol{q}_{vib,s} \cdot \boldsymbol{C}_s \left(\varepsilon_{vib,s} - \bar{\varepsilon}_{vib,s} \right) + \boldsymbol{\tau}_s : \boldsymbol{C}_s \boldsymbol{C}_s + P_{bulk,s} \left(\mathcal{C}_s^2 - \frac{3}{2} \right) + P_{rel,s} \left(\mathcal{C}_s^2 - \frac{3}{2} \right). \tag{36}$$

Finally, the GCE continuum breakdown parameters for the case of the two-temperature model are given by:

$$\boldsymbol{D}_{M,s} = \frac{2\beta_s \rho_s \boldsymbol{V}_{M,s}}{\rho_s} = \frac{2\beta_s \boldsymbol{D}_{M,s}^{NS}}{\rho_s},$$

$$\boldsymbol{D}_{T,s}^{(v)} = \frac{2\beta_s \rho_s \boldsymbol{V}_{T,s}^{(v)}}{\rho_s} = \frac{2\beta_s \boldsymbol{D}_{T,s}^{(v),NS}}{\rho_s},$$

$$\boldsymbol{D}_{T,s} = \frac{2\beta_s \rho_s \boldsymbol{V}_{T,s}}{\rho_s} = \frac{2\beta_s \boldsymbol{D}_{T,s}^{NS}}{\rho_s},$$

$$\boldsymbol{q}_{tr,s} = -\frac{4\beta_s}{5p_s} k_{tr,s} \nabla T_{tr} = \frac{4\beta_s \boldsymbol{q}_{tr,s}^{NS}}{5p_s},$$

$$\boldsymbol{q}_{rot,s} = -\frac{2\beta_s}{\rho_s c_{v,rot,s} T_{tr}} k_{rot,s} \nabla T_{tr} = \frac{2\beta_s \boldsymbol{q}_{rot,s}^{NS}}{\rho_s c_{v,rot,s} T_{tr}}, \tag{37}$$

$$\boldsymbol{q}_{vib,s} = -\frac{2\beta_s}{\rho_s c_{v,vib,s} T_{vib}} k_{vib,s} \nabla T_{vib} = \frac{2\beta_s \boldsymbol{q}_{vib,s}^{NS}}{\rho_s c_{v,vib,s} T_{vib}}$$

$$\boldsymbol{\tau}_s = \frac{2\mu_s}{p_s} \left(\frac{1}{2} \left(\nabla \mathbf{v} + \nabla^T \mathbf{v} \right) - \frac{1}{3} \nabla \cdot \mathbf{v} \mathbb{I} \right) = \frac{\boldsymbol{\tau}_s^{NS}}{p_s},$$

$$P_{bulk,s} = -\frac{1}{p_s} \zeta_s \nabla \cdot \mathbf{v} = \frac{p_{bulk,s}^{NS}}{p_s},$$

$$P_{rel,s} = \frac{p_{rel,s}^{NS}}{p_s}.$$

D. Three-temperature Model

In the three-temperature model, the energy exchange between T-T, R-R and V-V (intra-modal) are considered as fast processes, while T-R-V (inter-modal) energy exchange is a slow process. Owing to the fast intra-modal processes, the resulting translational, rotational and vibrational modes are assumed to follow Boltzmann distributions with distinct temperatures T_{tr}, T_{rot} and T_{vib}, but these temperatures are not necessarily in equilibrium owing to the slow T-R-V exchange. The corresponding characteristic time scales and fast and slow collision operators are thus:

$$\tau_{T-T} < \tau_{R-R} < \tau_{V-V} \ll \tau_{T-R-V} < \tau_{react} \sim \theta. \tag{38}$$

$$J^{rap} = J^{T-T} + J^{R-R} + J^{V-V},$$
$$J^{sl} = J^{T-R-V} + J^{react}. \tag{39}$$

For a mixture of gases following the three-temperature model with a rigid-rotor/harmonic oscillator assumption, the Generalized Chapman-Enskog (GCE) perturbation $\phi_{GCE,s}$ is of the form:

$$\phi_{GCE,s} = -\frac{1}{n} \mathbf{A}_s . \nabla ln(T_{tr}) - \frac{1}{n} \mathbf{A}_s^{(r)} \cdot \nabla ln(T_{rot}) - \frac{1}{n} \mathbf{A}_s^{(v)} \cdot \nabla ln(T_{vib})$$
$$- \frac{1}{n} \sum_t \mathbf{D}_s^t \cdot \boldsymbol{d}_t - \frac{1}{n} \mathbf{B}_s : \nabla \mathbf{v} - \frac{1}{n} \mathbf{G}_s. \tag{40}$$

The perturbation in the three-temperature model has two new terms $\mathbf{A}_s^{(r)}$ and $\mathbf{A}_s^{(v)}$ associated with the gradients in the rotational and vibrational temperatures. Since all inter-modal inelastic energy exchange processes are slow processes, the F_s term vanishes from Eq. 40. The polynomial expansion of the generalized functions are given by:

$$
\mathbf{A}_s = -\left(\frac{m_s}{2k_bT_{tr}}\right)^{1/2} \mathcal{C}_s \sum_r a_{s,r} \mathcal{S}_{3/2}^{(r)}\left(\mathcal{C}_s^2\right),
$$

$$
\mathbf{A}_s^{(r)} = -\left(\frac{m_s}{2k_bT_{tr}}\right)^{1/2} \mathcal{C}_s \sum_p a_{s,p}^{(r)} \mathcal{P}^{(p)}(\varepsilon_{rot,s}),
$$

$$
\mathbf{A}_s^{(v)} = -\left(\frac{m_s}{2k_bT_{tr}}\right)^{1/2} \mathcal{C}_s \sum_q a_{s,q}^{(v)} \mathcal{P}^{(q)}(\varepsilon_{vib,s}),
$$

$$
\mathbf{D}_s^t = \left(\frac{m_s}{2k_bT_{tr}}\right)^{1/2} \mathcal{C}_s \sum_r d_{s,r}^t \mathcal{S}_{3/2}^{(r)}\left(\mathcal{C}_s^2\right),
$$

$$
\mathbf{B}_s = \left(\mathcal{C}_s\mathcal{C}_s - \frac{1}{3}\mathcal{C}_s^2\mathbb{I}\right) \sum_r b_{s,r} \mathcal{S}_{3/2}^{(r)}\left(\mathcal{C}_s^2\right),
$$

$$
\mathrm{G}_s = -\sum_{rpq} g_{s,rpq} \mathcal{S}_{1/2}^{(r)}\left(\mathcal{C}_s^2\right) \mathcal{P}^{(p)}(\varepsilon_{rot,s}) \mathcal{P}^{(q)}(\varepsilon_{vib,s}).
$$

$$(41)$$

The transport coefficients are again expressed in terms of the polynomial expansion coefficients:

$$
k_{tr,s} = \frac{k_b}{3}\left[\mathbf{A}_s, \mathbf{A}_s\right] = \frac{5k_b}{4}\frac{n_s}{n}a_{s,1},
$$

$$
k_{rot,s} = \frac{k_b}{3}\left[\mathbf{A}_s^{(r)}, \mathbf{A}_s^{(r)}\right] = \frac{m_s c_{v,rot,s}}{2}\frac{n_s}{n}a_{s,1}^{(r)},
$$

$$
k_{vib,s} = \frac{k_b}{3}\left[\mathbf{A}_s^{(v)}, \mathbf{A}_s^{(v)}\right] = \frac{m_s c_{v,vib,s}}{2}\frac{n_s}{n}a_{s,1}^{(v)},
$$

$$
D_{T,s} = \frac{1}{3n}\left[\mathbf{D}_s^t, \mathbf{A}_s\right] = -\frac{1}{2n}a_{s,0},
$$

$$
D_{T,s}^{(r)} = \frac{1}{3n}\left[\mathbf{D}_s^t, \mathbf{A}_s^{(r)}\right] = -\frac{1}{2n}a_{s,0}^{(r)},
$$

$$
D_{T,s}^{(v)} = \frac{1}{3n}\left[\mathbf{D}_s^t, \mathbf{A}_s^{(v)}\right] = -\frac{1}{2n}a_{s,0}^{(v)},
$$

$$
D_{st} = \frac{1}{3n}\left[\mathbf{D}_s^t, \mathbf{D}_s^t\right] = \frac{1}{2n}d_{s,0}^t,
$$

$$
\mu_s = \frac{k_bT_{tr}}{10}\left[\mathbf{B}_s, \mathbf{B}_s\right] = \frac{k_bT_{tr}}{2}\frac{n_s}{n}b_{s,0},
$$

$$
\zeta_s = k_bT_{tr}\left[\mathrm{F}_s, \mathrm{F}_s\right] = 0,
$$

$$
p_{rel,s} = k_bT_{tr}\left[\mathrm{F}_s, \mathrm{G}_s\right] = 0.
$$

$$(42)$$

Note that in the three-temperature model, there are two additional thermal diffusion coefficients, arising from the separate rotational and vibrational temperatures. The bulk viscosity ζ and the relaxation pressure p_{rel} are equal to zero in this case due to the fact that there are no fast inter-modal inelastic processes. The perturbation function is next expressed in terms of the transport coefficients to obtain:

$$\mathbf{A}_s = \mathbf{A}_{s,T} + \mathbf{A}_{s,tr},$$

$$\mathbf{A}_s^{(r)} = \mathbf{A}_{s,T}^{(r)} + \mathbf{A}_{s,rot}^{(r)},$$

$$\mathbf{A}_s^{(v)} = \mathbf{A}_{s,T}^{(v)} + \mathbf{A}_{s,vib}^{(v)},$$

$$\mathbf{A}_{s,T} = \left(\frac{m_s}{2k_b T_{tr}}\right)^{1/2} 2n D_{T,s} \boldsymbol{\mathcal{C}}_s,$$

$$\mathbf{A}_{s,tr} = -\left(\frac{m_s}{2k_b T_{tr}}\right)^{1/2} \frac{4k_{tr,s}}{5k_b} \frac{n}{n_s} \left(\frac{5}{2} - \mathcal{C}_s^2\right) \boldsymbol{\mathcal{C}}_s,$$

$$\mathbf{A}_{s,T}^{(r)} = \left(\frac{m_s}{2k_b T_{tr}}\right)^{1/2} 2n D_{T,s}^{(r)} \boldsymbol{\mathcal{C}}_s,$$

$$\mathbf{A}_{s,rot}^{(r)} = -\left(\frac{m_s}{2k_b T_{tr}}\right)^{1/2} \frac{2k_{rot,s}}{m_s c_{v,rot,s}} \frac{n}{n_s} \left(\bar{\varepsilon}_{rot,s} - \varepsilon_{rot}\right) \boldsymbol{\mathcal{C}}_s, \tag{43}$$

$$\mathbf{A}_{s,T}^{(v)} = \left(\frac{m_s}{2k_b T_{tr}}\right)^{1/2} 2n D_{T,s}^{(v)} \boldsymbol{\mathcal{C}}_s,$$

$$\mathbf{A}_{s,vib}^{(v)} = -\left(\frac{m_s}{2k_b T_{tr}}\right)^{1/2} \frac{2k_{vib,s}}{m_s c_{v,vib,s}} \frac{n}{n_s} \left(\bar{\varepsilon}_{vib,s} - \varepsilon_{vib}\right) \boldsymbol{\mathcal{C}}_s,$$

$$\mathbf{D}_s^t = \left(\frac{m_s}{2k_b T_{tr}}\right)^{1/2} 2n D_{st} \boldsymbol{\mathcal{C}}_s,$$

$$\mathbf{B}_s = \frac{2\mu_s}{k_b T_{tr}} \frac{n}{n_s} \left(\boldsymbol{\mathcal{C}}_s \boldsymbol{\mathcal{C}}_s - \frac{1}{3}\mathcal{C}_s^2 \mathbb{I}\right),$$

$$\mathrm{G}_s = \frac{p_{rel,s}}{k_b T_{tr}} \frac{n}{n_s} \left(\frac{3}{2} - \mathcal{C}_s^2\right).$$

The diffusion velocity in the three-temperature model has four components owing to the mass diffusion and thermal diffusion from three temperature gradients:

$$\boldsymbol{V}_s = \boldsymbol{V}_{M,s} + \boldsymbol{V}_{T,s} + \boldsymbol{V}_{T,s}^{(r)} + \boldsymbol{V}_{T,s}^{(v)} = -\sum_t D_{st}\boldsymbol{d}_t - D_{T,s}\nabla ln(T_{tr}) - D_{T,s}^{(r)}\nabla ln(T_{rot}) - D_{T,s}^{(v)}\nabla ln(T_{vib}). \tag{44}$$

Expressing the diffusion terms using the diffusion velocity, the perturbation can be expressed as:

$$\begin{aligned}
\phi_{GCE,s} = {} & 2\beta_s \boldsymbol{V}_{M,s} \cdot \boldsymbol{\mathcal{C}}_s + 2\beta_s \boldsymbol{V}_{T,s} \cdot \boldsymbol{\mathcal{C}}_s + 2\beta_s \boldsymbol{V}_{T,s}^{(r)} \cdot \boldsymbol{\mathcal{C}}_s + 2\beta_s \boldsymbol{V}_{T,s}^{(v)} \cdot \boldsymbol{\mathcal{C}}_s \\
& - \frac{4\beta_s k_{tr,s}}{5p_s} \left(\mathcal{C}_s^2 - \frac{5}{2}\right) \boldsymbol{\mathcal{C}}_s \cdot \nabla T_{tr} \\
& - \frac{2\beta_s k_{rot,s}}{\rho_s c_{v,rot,s} T_{rot}} \left(\varepsilon_{rot,s} - \bar{\varepsilon}_{rot,s}\right) \boldsymbol{\mathcal{C}}_s \cdot \nabla T_{rot} \\
& - \frac{2\beta_s k_{vib,s}}{\rho_s c_{v,vib,s} T_{vib}} \left(\varepsilon_{vib,s} - \bar{\varepsilon}_{vib,s}\right) \boldsymbol{\mathcal{C}}_s \cdot \nabla T_{vib} \\
& - \frac{2\mu_s}{p_s} \boldsymbol{\mathcal{C}}_s \boldsymbol{\mathcal{C}}_s : \left(\frac{1}{2}\left(\nabla \mathbf{v} + \nabla^T \mathbf{v}\right) - \frac{1}{3}\nabla \cdot \mathbf{v}\mathbb{I}\right).
\end{aligned} \tag{45}$$

The Generalized Chapman-Enskog perturbation $\phi_{GCE,s}$ for the three-temperature model is expressed in terms of flux-based quantities as:

$$\begin{aligned}
\phi_{GCE,s} = {} & \boldsymbol{D}_{M,s} \cdot \boldsymbol{\mathcal{C}}_s + \boldsymbol{D}_{T,s} \cdot \boldsymbol{\mathcal{C}}_s + \boldsymbol{D}_{T,s}^{(r)} \cdot \boldsymbol{\mathcal{C}}_s + \boldsymbol{D}_{T,s}^{(v)} \cdot \boldsymbol{\mathcal{C}}_s + \boldsymbol{q}_{tr,s} \cdot \boldsymbol{\mathcal{C}}_s \left(\mathcal{C}_s^2 - \frac{5}{2}\right) \\
& + \boldsymbol{q}_{rot,s} \cdot \boldsymbol{\mathcal{C}}_s \left(\varepsilon_{rot,s} - \bar{\varepsilon}_{rot,s}\right) + \boldsymbol{q}_{vib,s} \cdot \boldsymbol{\mathcal{C}}_s \left(\varepsilon_{vib,s} - \bar{\varepsilon}_{vib,s}\right) + \boldsymbol{\tau}_s : \boldsymbol{\mathcal{C}}_s \boldsymbol{\mathcal{C}}_s.
\end{aligned} \tag{46}$$

Thus the GCE continuum breakdown parameters for the three-temperature model are:

$$
\begin{aligned}
\boldsymbol{D}_{M,s} &= \frac{2\beta_s\rho_s\boldsymbol{V}_{M,s}}{\rho_s} = \frac{2\beta_s\boldsymbol{D}_{M,s}^{NS}}{\rho_s}, \\[4pt]
\boldsymbol{D}_{T,s} &= \frac{2\beta_s\rho_s\boldsymbol{V}_{T,s}}{\rho_s} = \frac{2\beta_s\boldsymbol{D}_{T,s}^{NS}}{\rho_s}, \\[4pt]
\boldsymbol{D}_{T,s}^{(r)} &= \frac{2\beta_s\rho_s\boldsymbol{V}_{T,s}^{(r)}}{\rho_s} = \frac{2\beta_s\boldsymbol{D}_{T,s}^{(r),NS}}{\rho_s}, \\[4pt]
\boldsymbol{D}_{T,s}^{(v)} &= \frac{2\beta_s\rho_s\boldsymbol{V}_{T,s}^{(v)}}{\rho_s} = \frac{2\beta_s\boldsymbol{D}_{T,s}^{(v),NS}}{\rho_s}, \\[4pt]
\boldsymbol{q}_{tr,s} &= -\frac{4\beta_s}{5p_s}k_{tr,s}\nabla T_{tr} = \frac{4\beta_s\boldsymbol{q}_{tr,s}^{NS}}{5p_s}, \\[4pt]
\boldsymbol{q}_{rot,s} &= -\frac{2\beta_s}{\rho_s c_{v,rot,s}T_{rot}}k_{rot,s}\nabla T_{rot} = \frac{2\beta_s\boldsymbol{q}_{rot,s}^{NS}}{\rho_s c_{v,rot,s}T_{rot}}, \\[4pt]
\boldsymbol{q}_{vib,s} &= -\frac{2\beta_s}{\rho_s c_{v,vib,s}T_{vib}}k_{vib,s}\nabla T_{vib} = \frac{2\beta_s\boldsymbol{q}_{vib,s}^{NS}}{\rho_s c_{v,vib,s}T_{vib}}, \\[4pt]
\boldsymbol{\tau}_s &= \frac{2\mu_s}{p_s}\left(\frac{1}{2}\left(\nabla\mathbf{v}+\nabla^T\mathbf{v}\right)-\frac{1}{3}\nabla\cdot\mathbf{v}\mathbb{I}\right) = \frac{\boldsymbol{\tau}_s^{NS}}{p_s}.
\end{aligned}
\tag{47}
$$

E. Comparison with the Kn$_{GLL}$ Breakdown Parameters

In this section, an analytical comparison between the GCE and GLL continuum breakdown parameters is made. The comparison is limited to the translational heat flux and (self) difussion flux for a single species gas. As will be seen in Section IV, these are the primary mechanisms leading to breakdown in the reacting flow case presented in this work, but this analysis can be readily extended to facilitate comparison between other breakdown parameter quantities.

1. Translational heat flux

The GCE and GLL breakdown parameters that predict continuum breakdown associated with large gradients in translational temperature (i.e., heat flux) are the translational heat flux breakdown parameter (GCE) and the Gradient-Length-Local (GLL) Knudsen number based on translational temperature (repeated from Eq. 47 and Eq. 2):

$$
\boldsymbol{q}_{tr,GCE} = -\frac{4\beta}{5p}k_{tr}\nabla T_{tr}
\tag{48}
$$

$$
Kn_{GLL}^{T,tr} = \frac{\lambda_{mfp}}{T}\nabla T_{tr}
\tag{49}
$$

Substituting $\beta = \sqrt{m/2k_bT_{tr}}$, $p = nk_bT_{tr}$ and expressing both the translational thermal conductivity and mean free path of a single-species gas in terms of Ω integrals:

$$
k_{tr} = \frac{25c_{v,tr}k_bT_{tr}}{16\Omega^{(2,2)}},
\tag{50}
$$

$$
\lambda_{mfp} = \frac{1}{n\Omega^{(2,2)}}\sqrt{\frac{2k_bT_{tr}}{\pi m}},
\tag{51}
$$

the ratio of the breakdown parameters is determined as:

$$\frac{\boldsymbol{q}_{tr,GCE}}{Kn_{GLL}^{T,tr}} = \frac{15\sqrt{\pi}}{16}. \tag{52}$$

This ratio indicates that the GCE and GLL continuum breakdown parameters associated with translational temperature gradients are not equivalent, but are different by a constant factor of $15\sqrt{\pi}/16$ (≈ 1.66). This factor is precisely the normalization constant that originates from the Sonine polynomial integration during the evaluation of the bracket integral $[\mathbf{A}, \mathbf{A}]$, i.e., a result from kinetic theory. It should be noted that this ratio becomes significantly more complex for a gas mixture, as Eq. 50 becomes a system of equations involving mixture composition [7].

2. Self-diffusion flux

The GCE and GLL breakdown parameters that predict continuum breakdown associated with large gradients in species concentration (i.e., diffusion flux) are the diffusion flux breakdown parameter (GCE) and the Gradient-Length-Local (GLL) Knudsen number based on species density:

$$\boldsymbol{D}_{M,s} = 2\beta \boldsymbol{V}_{M,s} = 2\beta D_{ss} \boldsymbol{d}_s \tag{53}$$

$$Kn_{GLL}^{\rho_s} = \frac{\lambda_{mfp}}{\rho_s} \nabla \rho_s \tag{54}$$

Self-diffusion is presented here to facilitate comparison, as the analysis becomes increasingly more complex for multi-component diffusion in gas mixtures. For the case of self-diffusion, the diffusion coefficient and the driving force can be expressed as:

$$D_{ss} = \frac{3k_b T_{tr}}{8nm\Omega^{(1,1)}} \tag{55}$$

$$\boldsymbol{d}_s = \frac{\nabla \rho_s}{\rho_s} \tag{56}$$

Substituting these expressions and the definition of λ_{mfp} from Eq. 51, the ratio of the breakdown parameters is obtained as:

$$\frac{\boldsymbol{D}_{M,s}}{Kn_{GLL}^{\rho_s}} = \frac{3\sqrt{\pi}}{8} \frac{\Omega^{(2,2)}}{\Omega^{(1,1)}} \tag{57}$$

The GCE and GLL diffusion breakdown parameters are also not equivalent, but in this case their ratio is a variable function of the $\Omega^{(1,1)}$ and $\Omega^{(2,2)}$ collision integrals. This is due to the fact that diffusion, which appears in the GCE parameter, is associated with the transport of mass or identity (represented by $\Omega^{(1,1)}$), while the mean free path, which appears in the GLL parameter, is associated with the transport of momentum or energy (represented by $\Omega^{(2,2)}$). The factor of $3\sqrt{\pi}/8$ appearing on the right-hand side of Eq. 57 is the normalization constant associated with the bracket integral of $[\mathbf{D}_s^t, \mathbf{D}_s^t]$, again a result from kinetic theory. This suggests that the GLL breakdown parameters, which are expressed in terms of a Knudsen number based on a length scale determined by flow gradients [9], does not properly capture the true departure of the distribution function from equilibrium as determined by the Generalized Chapman-Enskog method (a precursor to the Navier-Stokes equations) and kinetic theory.

IV. ASSESSMENT OF CONTINUUM BREAKDOWN

The GCE breakdown parameters developed in the preceding sections are analyzed for a hypersonic flow past a sphere. Translational and vibrational heat flux, species diffusion and stress tensor breakdown parameters are evaluated at each point in the flow field to determine the mechanisms responsible for continuum breakdown at a given location.

The GCE breakdown parameters are then compared with the corresponding GLL parameters to elucidate: (i) the spatial variation, if any, in the predicted onset of continuum breakdown, and (ii) the physical mechanisms responsible for continuum breakdown in either case. Furthermore, the relative strengths of competing mechanisms are assessed to identify the physical processes which drive the system towards non-equilibrium, and collisional processes that work to restore equilibrium.
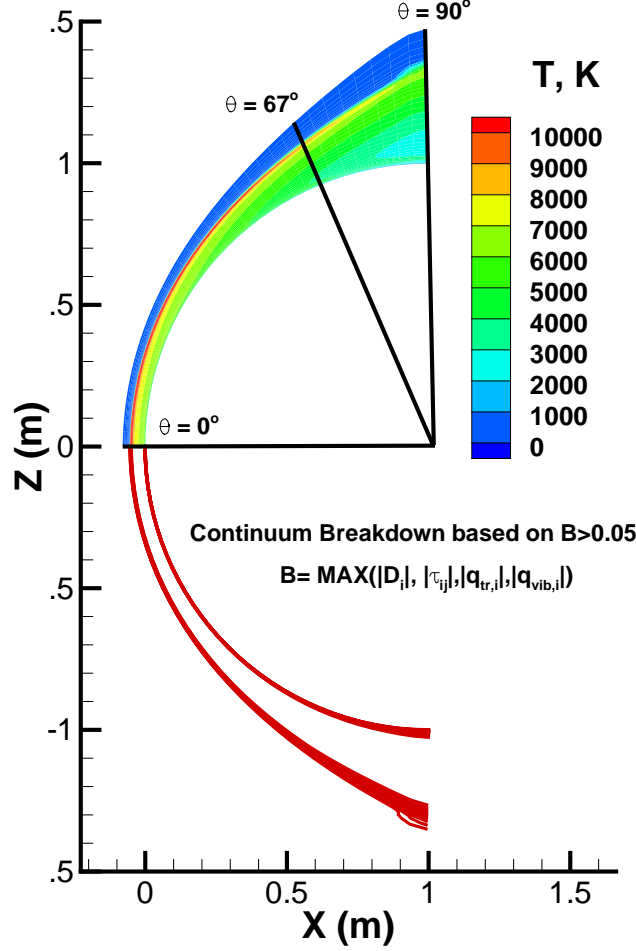
A.   Computational Setup

FIG. 1. The computational domain: temperature contours (top); GCE continuum breakdown regions based on a threshold of 0.05 (bottom). Black lines indicate flow field profiles extracted for analysis at $\theta = 0°$, $67°$ and $90°$.

Two-dimensional, reacting air flow past a sphere is simulated using the finite volume, implicit Langley Aerothermodynamic Upwind Relaxation Algorithm (LAURA) (Fig. 1) [20, 21]. The system is modeled as an 11-species air mixture with free-stream conditions as shown in Table I. The sphere surface is treated as a fully catalytic wall with radiative equilibrium wall temperature. A no-slip velocity boundary condition is enforced on the sphere surface. Chemical reactions are modeled using Park's finite rate chemistry for the entire flow field. The two-temperature model is used in which the rotational and translational modes are assumed to be in equilibrium, and translational-vibrational non-equilibrium is modeled via the Landau-Teller formulation. Species-wise diffusion coefficients are obtained from the self-consistent effective binary diffusion coefficient (SCEBD) model [22, 23] and mixture viscosity, translational and internal thermal conductivities are obtained from the Gupta-Yos mixing rule [24].

TABLE I. Free stream conditions.

Parameter	Value
M	24
ρ	1e-4 [kg/m^3]
T	276 [K]
u	8000 [m/s]
χ_{N_2}	0.7835
χ_{O_2}	0.2165

B. GCE Continuum Breakdown

(a)

(b)

(c)
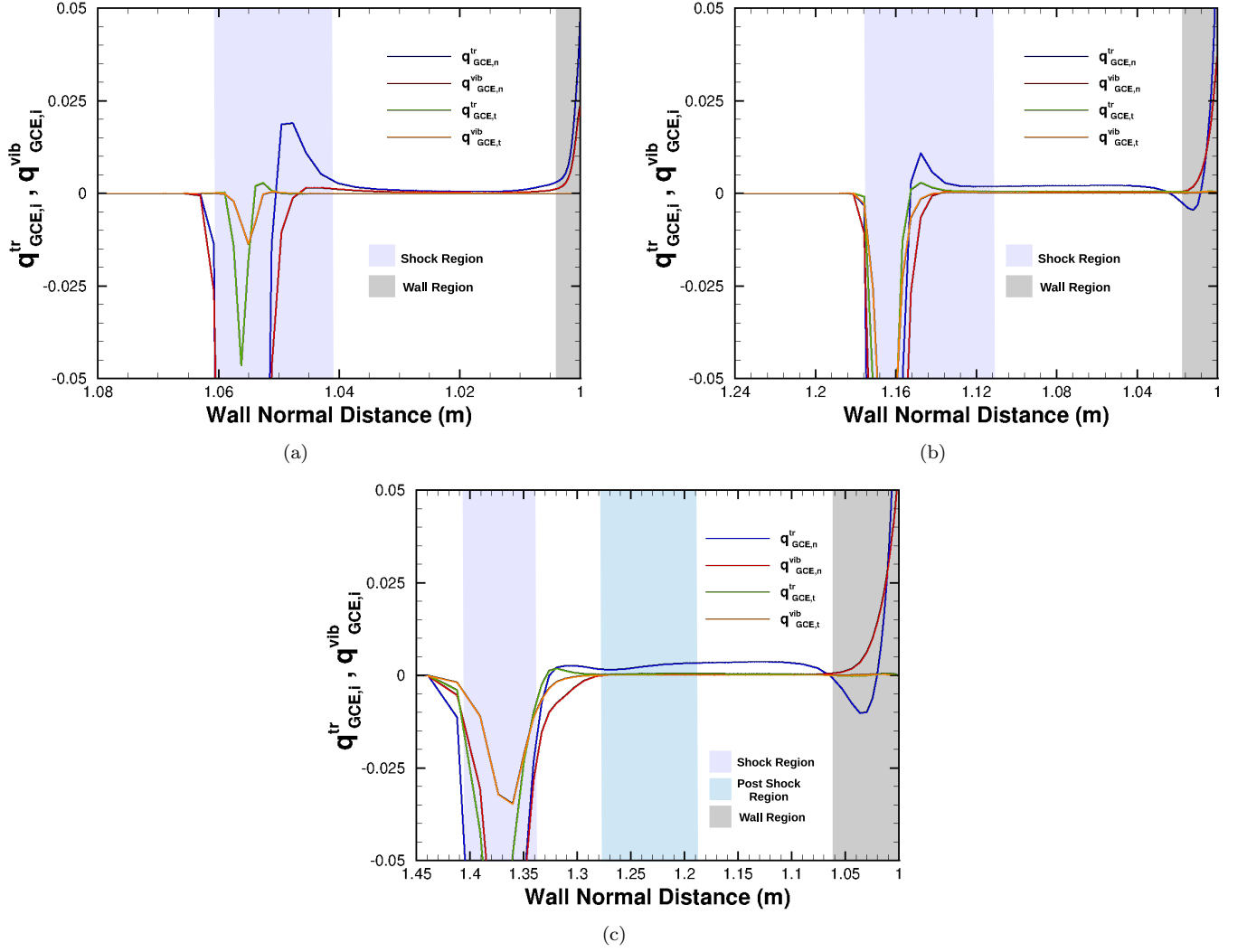
FIG. 2. Translational and vibrational heat flux breakdown parameters along: (a) $\theta = 0°$ (stagnation line), (b) $\theta = 67°$, (c) $\theta = 90°$ profiles as indicated in Fig. 1. Note the variation in the range of the wall-normal distance from (a) to (c). The shaded regions indicate continuum breakdown as specified in Eq. 58.

The focus of this analysis is aimed toward an understanding of the breakdown mechanisms in the shock region and near the sphere surface. The breakdown parameters for a two-temperature model presented in Section III C are assessed along profiles at $\theta = 0°$, 67° and 90° (Fig. 1), starting from just upstream of the bow shock and extending to the surface of the sphere. Both the normal and tangential components of the breakdown parameters are computed at each angular position. The diffusion breakdown parameter is evaluated for each component of the 11-species air

mixture according to the SCEBD formulation of species diffusion flux [22]. However, it should be noted that multi-component diffusion breakdown parameters should be computed if the pairwise diffusion coefficients are available. The translational and vibrational heat flux and stress tensor breakdown parameters have been calculated for the mixture as a whole, but these quantities may also be computed per species. The LAURA solver does not include thermal diffusion, bulk viscosity or relaxation pressure in the governing equations, so these are omitted from the current analysis. Thus, the continuum breakdown parameters computed for this problem include:

$$B = \text{MAX}(|D_i^s|, |\tau_{ij}|, |q_i^{tr}|, |q_i^{vib}|), \tag{58}$$

each evaluated in terms of the wall-normal and tangential components. The breakdown criterion of $B = 0.05$ is adopted from the Kn_{GLL} criterion for this analysis to facilitate comparison [9]. The continuum breakdown parameters are plotted in Figs. 2 – 3 as a function of wall-normal distance at each angular position. The shaded regions in each figure indicate regions of GCE continuum breakdown based on the definition in Eq. 58, which include breakdown within the shock region and the near-surface region, where gradients and consequently, the fluxes are highest.

1. Heat flux breakdown

The wall normal and tangential components of the translational and vibrational heat flux breakdown parameters are shown in Fig. 2 along $\theta = 0°$, $67°$ and $90°$. Following the profiles from left (freestream) to right (sphere wall), the first shaded region represents the non-continuum region at the shock, and the second indicates the presence of a non-continuum region near the sphere surface. Along the $\theta = 90°$ profile, a third 'post shock' breakdown region is observed due to high diffusion fluxes of NO, O_2, and will be discussed in the next subsection. Within each of these regions, at least one of the continuum breakdown parameters have crossed the breakdown threshold of 0.05, indicating that a kinetic scheme must be employed to accurately describe the flow field.

Along all the three angular positions considered namely, $\theta = 0°$, $67°$ and $90°$, the heat flux parameters initiate continuum breakdown at the shock region. Thus, within the shock, the steep gradients in the translational and vibrational temperatures and the resulting heat fluxes are responsible for perturbing the equilibrium Maxwellian VDF of the system. The 'end-of-shock' breakdown location marks the end of the shaded region around the shock, after which all breakdown parameters are within the breakdown threshold, and the Navier-Stokes equations may be used to compute system properties until the start of the next breakdown region is encountered. The 'end-of-shock' is indicated by the species-wise diffusion breakdown parameter along each angular position considered. (Table II).

Along the $\theta = 0°$ and $67°$ locations, continuum region beyond the 'end-of-shock' location extends until ~4mm and ~17mm upstream of the sphere surface respectively. Similarly, in case of the $\theta = 90°$ position, the continuum region downstream of the 'post shock region' (Fig. 2 (c)) terminates when breakdown is observed near the sphere surface. Along all three angular positions, the near wall breakdown is determined by the species-wise diffusion fluxes, as discussed in the following sub section. Although the heat flux parameters do not determine the onset of breakdown near the wall, the normal components of the translational and vibrational heat flux breakdown parameters do cross the breakdown threshold very close of the sphere surface, along the $\theta = 67°$ and $90°$ positions. The sharp temperature gradients that are setup due to the hot gases from the shock layer approaching the relatively cool sphere surface, are responsible for this effect

Further, Fig. 2 also reveals that with increasing angular positions, the near wall breakdown of the heat flux parameter occurs further upstream of the sphere surface. Since the heat flux breakdown parameters are normalized by pressure (Eq. 37), this trend observed in the breakdown location of the heat flux terms is likely due to the decreasing pressure near the sphere surface with increasing angular position, from the stagnation line ($\theta = 0°$) to the sphere shoulder ($\theta = 90°$).

2. Diffusion breakdown

Fig. 3 shows the GCE diffusion breakdown parameters along $\theta = 0°$, $67°$ and $90°$. The most prominent diffusion breakdown parameters are the wall normal components for N_2, O_2, N, O and NO, while the tangential components (not shown) are not significant in determining any breakdown location. For similar reasons, the diffusion breakdown parameters of charged species have not been shown.

The diffusion flux required to compute the species-wise diffusion breakdown parameter has been evaluated using the SCEBD model of Ramshaw[22]. The diffusion breakdown parameter (Eq. 37) is computed as the species diffusion flux normalized by the inverse most probable speed of the species and the species density, ρ_s. In case of a chemically
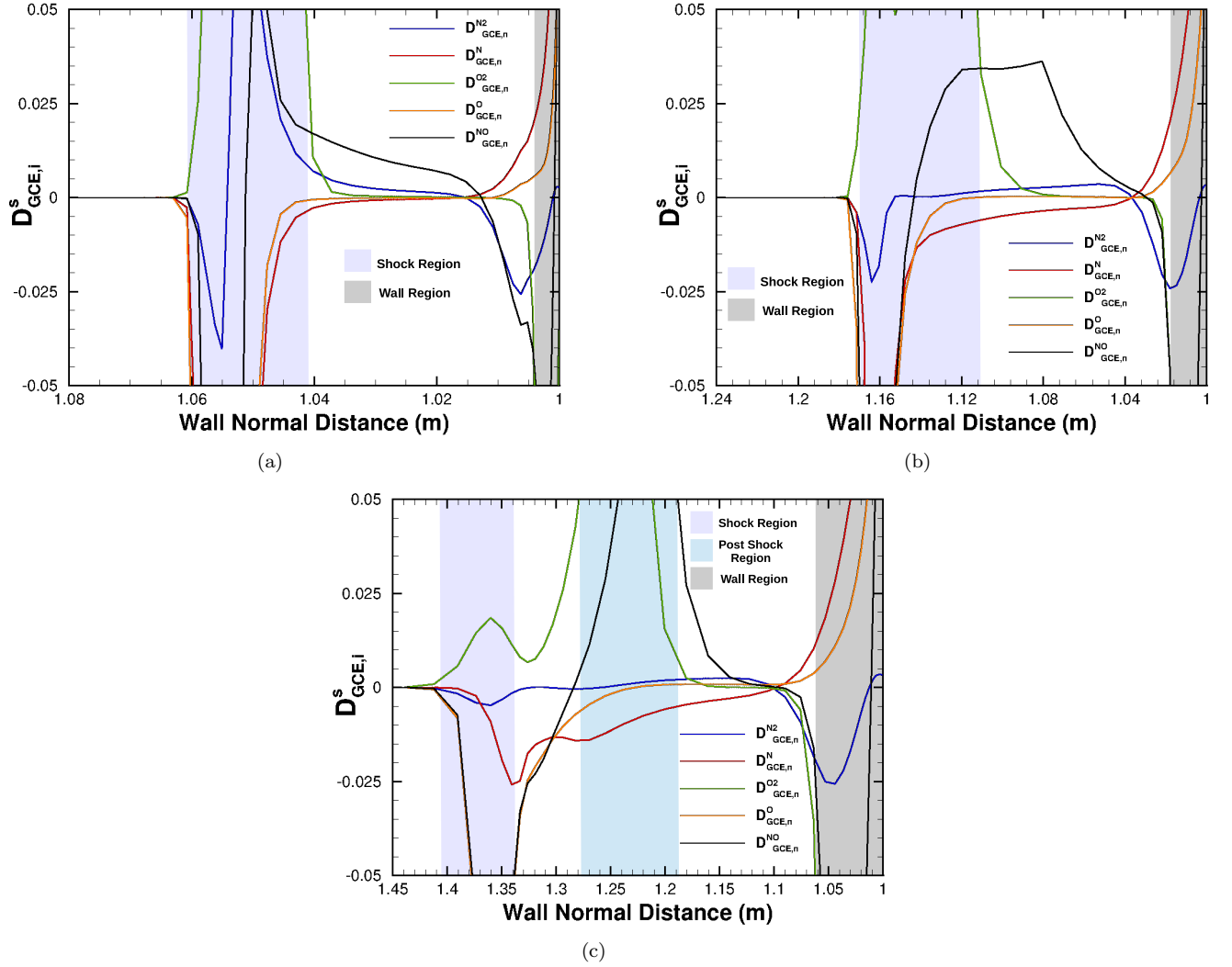
FIG. 3. Diffusion breakdown parameters along (a) $\theta = 0°$ (stagnation line), (b) $\theta = 67°$, (c) $\theta = 90°$ profiles indicated in Fig. 1. Note the variation in the range of the wall-normal distance from (a) to (c). The shaded regions indicate continuum breakdown as specified in Eq. 58.

reacting flow with conditions enabling complete dissociation/recombination, the ρ_s falls to very low values at certain locations in the flow field. This leads to mathematical anomalies in the computation of $D^s_{GCE,i}$. To overcome this, the ρ_s in Eqn. 37 is set to $max(\rho_s, 0.001 * \rho_{total})$ where ρ_{total} is the total density at the location under consideration.

Following the $\theta = 0°$ and $\theta = 67°$ profile from left (free stream) to right (toward the surface), Fig. 3 (a), (b) indicate that diffusion fluxes have become significant at the start of shock breakdown location. However, at the sphere shoulder ($\theta = 90°$), diffusion fluxes become significant only after continuum breakdown has already been initiated by the heat flux parameters (Fig. 2 (c)). The 'end-of-shock' breakdown location along all three angular positions is governed by the diffusion breakdown parameter. Steep species concentration gradients are observed in the shock. These gradients, coupled with the rise in pressure that accompanies the shock, contribute to the diffusion driving force (Eq. 19) that is responsible for distorting the Maxwellian VDF of the system by means of large species diffusion fluxes. Further, the decreasing peak shock temperatures with increasing angular positions cause reactions to occur until downstream of the shock. This results in extending the 'end-of-shock' breakdown location further downstream of the actual shock. The 'post shock' breakdown region that is observed along $\theta = 90°$ is likely to develop due to the same reason.

In approaching the sphere surface, it is the species diffusion breakdown parameter ($D^{O2}_{GCE,n}$) that determines the onset of the near wall breakdown region. The movement of hot fluid towards the relatively cold sphere surface creates temperature gradients that initiate gas phase reactions. Coupled with wall catalycity effects, steep concentration gradients develop that lead to large diffusion fluxes. Although recombinations of N begin further upstream of the wall along all three angular positions, the diffusion fluxes of O_2 determine the start of the near wall breakdown region.

Unlike N_2, O_2 is almost completely dissociated in the shock. Therefore the concentration of O_2 in moving towards the wall is very low. The low concentration along with the rise in diffusion flux of O_2 due to chemical reactions in the wall vicinity, distort the VDF, leading to continuum breakdown.

Fig. 3 also reveals that with increasing angular positions, the near wall breakdown of the species-wise diffusion parameter occurs at larger distances upstream of the sphere surface. This can be attributed to the decreasing total density (and hence, species density) as one traverses along the sphere surface from the stagnation line to the sphere shoulder.

(a)

(b)

(c)
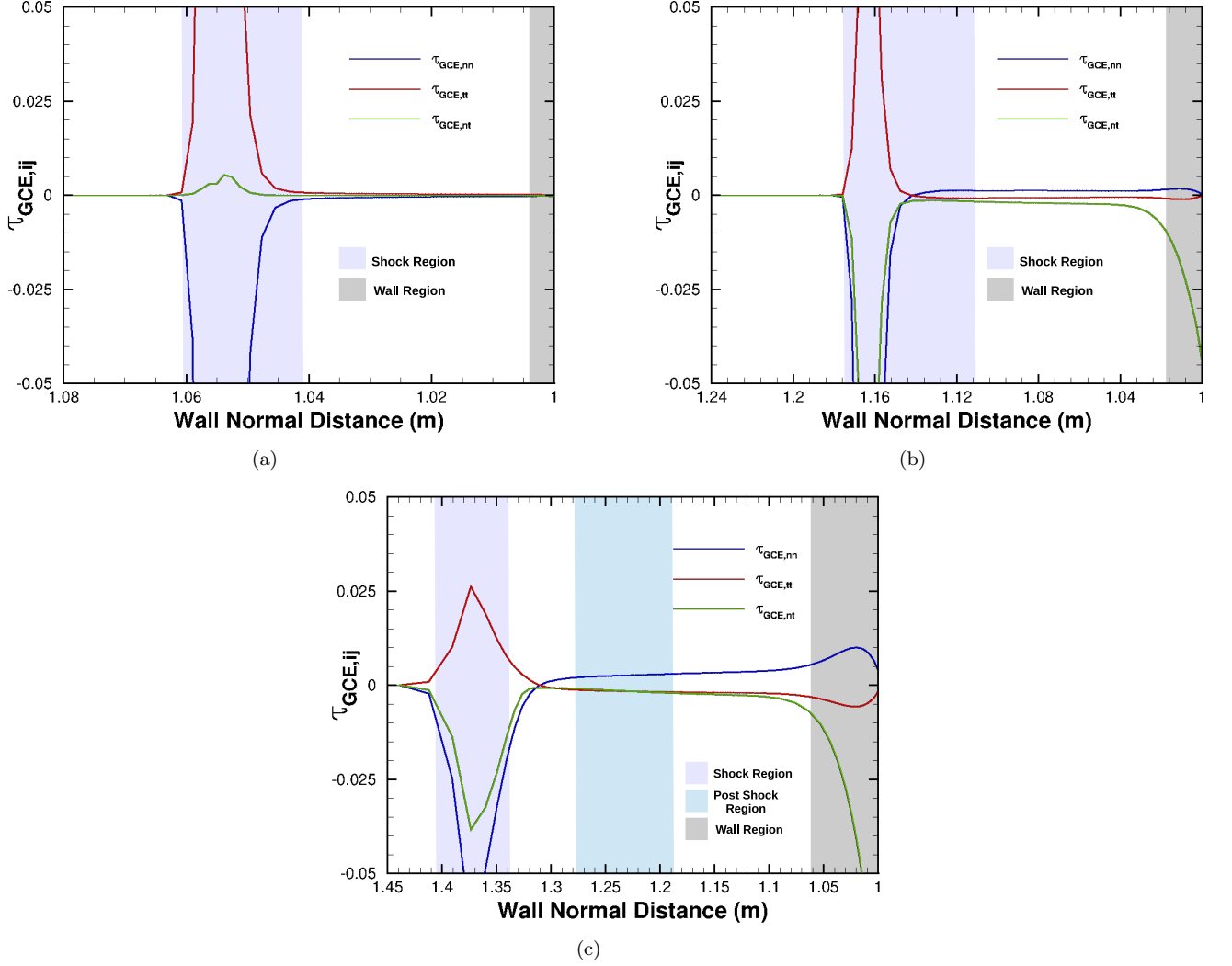
FIG. 4. Stress Tensor breakdown parameters along: (a) $\theta = 0°$ (stagnation line), (b) $\theta = 67°$, (c) $\theta = 90°$ profiles indicated in Fig. 1. Note the variation in the range of the wall-normal distance from (a) to (c). The shaded regions indicate continuum breakdown as specified in Eq. 58.

3. Stress tensor breakdown

Fig. 4 shows the normal (nn), tangential (tt) and shear (nt) stress breakdown parameters along $\theta = 0°$, $67°$ and $90°$. Following the profiles from left to right, it can be seen that continuum breakdown occurs at the shock region before the stress components become significant. With an increase in the angular position, the value of the stress tensor components close to the sphere wall begins to increase. The sharp velocity gradients developed due to the slowing of the fluid in the wall boundary layer are responsible for this rise. However, the stress tensor breakdown parameters do not determine any of the breakdown locations.

It is clear from Figs. 2 – 3 that there exist two (three for $\theta = 90°$) distinct continuum breakdown regions (shock, post-shock and near the sphere surface) where transition needs to be made from a CFD to a kinetics-based solution technique. This transition, often referred to as the hybrid interface location introduced in Section I, is determined by the location where any of the breakdown parameter values has exceeded the breakdown threshold. The physical mechanisms leading to the onset of continuum breakdown are summarized in Table II for the cases considered above. The shock (and post-shock) region is bound by two separate hybrid interfaces, one defining 'start-of-shock' continuum breakdown location and the second, defining the 'end-of-shock' continuum breakdown location, while the breakdown near the sphere surface is governed by a single hybrid interface. Multiple breakdown parameters are listed for cases where multiple mechanisms simultaneously predict continuum breakdown. For the 'post shock' breakdown region developed along $\theta = 90°$, the interfaces are governed by $D_n^{O_2}$, D_n^{NO} and have not been listed in the table below.

TABLE II. Breakdown Mechanisms: 2-d flow over sphere.

Angle	Start-shock region	End-of-shock region	Wall region
0	q_n^{tr}, q_n^{vib}, D_n^{O}, D_n^{N}	$D_n^{O_2}$	$D_n^{O_2}$, D_n^{NO}
67	q_n^{tr}, q_n^{vib}, D_n^{O}, D_n^{NO}	$D_n^{O_2}$	$D_n^{O_2}$, D_n^{NO}
90	q_n^{tr}	D_n^{O}, D_n^{NO}	$D_n^{O_2}$

C.   Chemical reactions: Indirect Influence on Continuum Breakdown

Table II and Fig. 3 (a) reveal that in the near wall region along the stagnation line, continuum breakdown is initiated by the diffusion breakdown parameter, $D_n^{O_2}$. This section elucidates the competition between the physical mechanisms that drive the system towards non-equilibrium, as well as mechanisms that work to restore the system back to equilibrium.
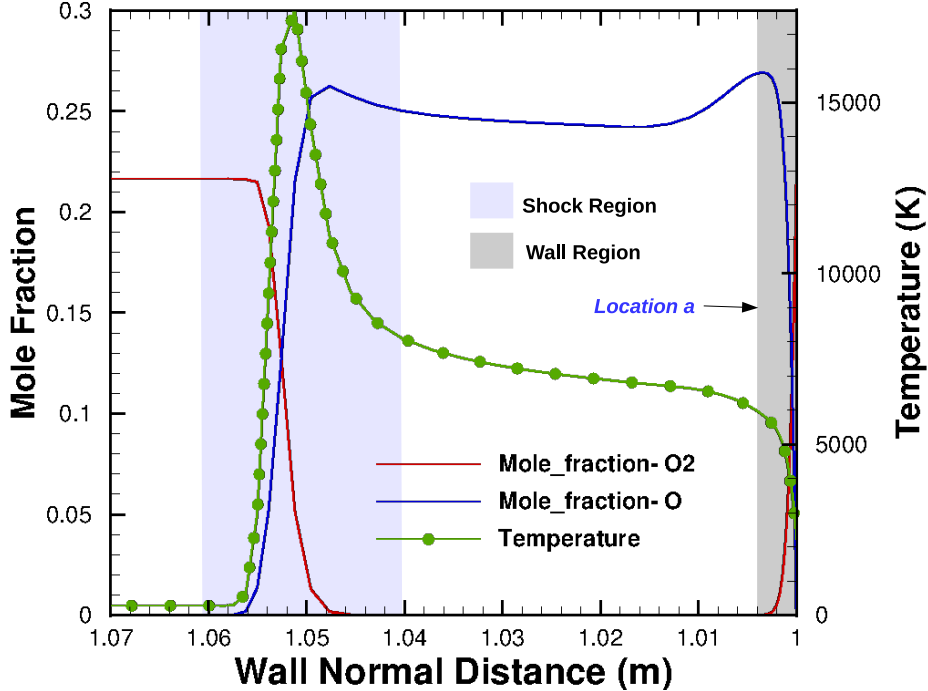

FIG. 5. Variation in temperature and mole fraction of O_2 and O in the flow field along the stagnation line.

Consider, for example, the temperature and mole fractions of O and O_2 along the stagnation line leading up to the sphere surface. Compared to the hot gas ($\sim$7000 K) in the post shock layer, the relatively cool wall temperature of 2200 K is expected to decrease the gas-phase dissociation of O_2, partially contributing to the observed decrease in

the mole fraction of O and increase in mole fraction of O_2 near the wall (Fig. 5). Further, the advection and diffusion processes, coupled with wall catalycity effects result in a high rate of surface recombination. These recombination reactions form O_2, leading to a strong flux of O_2 away from the wall, with the wall acting as a source. Thus, advection and diffusion of O towards the wall produces O_2 through gas-surface recombinations, which in turn leads to diffusion of O_2 away from the wall. The final, steady state composition of the gas near the wall depends of the relative balance between the competing physical mechanisms in this region, namely advection, diffusion and gas-phase and gas-surface recombination reactions. With this view, the first and second Damköhler numbers Da_I and Da_{II} respectively, have been evaluated as [25]:

$$Da_I = \frac{\tau_{advection}}{\tau_{react}} \tag{59}$$

$$Da_{II} = \frac{\tau_{diffusion}}{\tau_{react}} \tag{60}$$

at two locations along the stagnation line: (i) at the start of the near wall breakdown region ($\sim$4mm upstream of the sphere surface, Fig. 5) henceforth, referred to as *Location a* and (ii) at the sphere surface. Thus, Da_I compares the advection and reaction time scales, whereas Da_{II} relates the diffusion and reaction time scales. The ratio of Da_I to Da_{II} therefore serves as an indicator of whether the advection or diffusion process dominates in a chosen region of the flow field.

Using the general definition of Damköhler numbers as per Eqs. 59 and 60, three sets of Damköhler numbers, Da_I and Da_{II}, (six Damköhler numbers in all) have been evaluated. The first set compares the time scales of: (i) advection with gas-phase reactions at *Location a* ($Da_{I,\text{gas}}$) and (ii) diffusion with gas-phase reaction at *Location a* ($Da_{II,\text{gas}}$). The second set compares the time scales of: (i) advection with surface reactions at the sphere wall ($Da_{I,\text{surf}-w}$) and (ii) diffusion with surface reactions at the sphere wall ($Da_{II,\text{surf}-w}$). The third set compares the time scales of: (i) advection with 'effective' surface reactions at *Location a* ($Da_{I,\text{surf}-a}$) and (ii) diffusion with 'effective' surface reactions at *Location a* ($Da_{II,\text{surf}-a}$).

The first set of Damköhler numbers which is used to assess the relative strength of the diffusion and advection process with respect to gas-phase recombinations, is evaluated at *Location a* as:

$$Da_{I,\text{gas}} = \frac{\dot{w}_s l_d}{\rho_s |V|} \tag{61}$$

$$Da_{II,\text{gas}} = \frac{\dot{w}_s l_d{}^2}{\rho_s D_s} \tag{62}$$

where $\dot{w}_s$ is the species production due to gas-phase dissociation and recombination, and ρ_s denotes species density. The quantity l_d is the characteristic diffusion length, and is taken to be the distance from the sphere wall to *Location a* ($\sim$4mm) for computing all six Damköhler numbers. The quantities $|V|$ and D_s denote the velocity magnitude, and the diffusion coefficient of the species under consideration at *Location a*. For all the quantities computed in this analysis, atomic oxygen, O is the species of interest. The values of $Da_{I,\text{gas}}$ and $Da_{II,\text{gas}}$, computed at *Location a*, as per Eq. 61 and Eq. 62 are presented in the first row of Table III.

The second set of Damköhler numbers are evaluated at the sphere wall, and provide an assessment of the relative strengths of advection and diffusion of O with respect to surface recombinations of O. These numbers are formulated as:

$$Da_{I,\text{surf}-w} = \frac{1}{|V|} \gamma_w \sqrt{\frac{k_B T_w}{2\pi m_s}} \tag{63}$$

$$Da_{II,\text{surf}-w} = \frac{l_d}{D_s} \gamma_w \sqrt{\frac{k_B T_w}{2\pi m_s}} \tag{64}$$

where T_w and m_s are the wall temperature and the particle weight of the atomic species [26]. γ_w is the surface catalycity, and for the fully catalytic wall considered in this work, $\gamma_w = 1$. It should be noted that both $|V|$ and D_s are values of velocity magnitude and species-wise diffusion coefficient respectively, at the sphere wall. The values of $Da_{I,\mathrm{surf-w}}$ and $Da_{II,\mathrm{surf-w}}$, computed at the sphere wall, as per Eq. 63 and Eq. 64 are presented in the second row of Table III.

The third set of Damköhler numbers are evaluated again at *Location a*, and provide an assessment of the relative strength of advection and diffusion of O with respect to an 'effective' surface recombinations of O. To translate the influence of surface reactions occurring at the sphere wall to *Location a*, Thoemel *et al.* [26] has suggested the use of an 'effective' wall catalycity, $\gamma_{effective}$ given by:

$$\gamma_{effective} = \frac{Net\ recombination\ flux\ of\ O\ at\ Location\ a}{Total\ flux\ of\ O\ at\ Location\ a} \qquad (65)$$

Based on this effective wall catalycity, $Da_{I,\mathrm{surf-a}}$ and $Da_{II,\mathrm{surf-a}}$ can be expressed as:

$$Da_{I,\mathrm{surf-a}} = \frac{1}{|V|}\gamma_{effective}\sqrt{\frac{k_B T_a}{2\pi m_s}} \qquad (66)$$

$$Da_{II,\mathrm{surf-a}} = \frac{l_d}{D_s}\gamma_{effective}\sqrt{\frac{k_B T_a}{2\pi m_s}} \qquad (67)$$

where T_a, $|V|$, D_s are values of gas temperature, velocity magnitude and species-wise diffusion coefficient respectively, at *Location a*. The values of $Da_{I,\mathrm{surf-a}}$ and $Da_{II,\mathrm{surf-a}}$, computed using Eq. 66 and Eq. 67, are presented in the third row of Table III. Thus, a time scale comparison for each of the competing mechanisms that can influence continuum breakdown in the vicinity of the sphere wall namely – advection, diffusion, gas phase reactions and surface recombinations – has been summarized in the form of Damköhler numbers, based on Eq. 61 - 67 in Table III.

TABLE III. Time scale comparison between diffusion, advection, gas-phase and surface chemistry.

Position	Reaction considered	Da_I	Da_{II}
Location a (Eqs.61, 62)	Gas phase	0.000181	0.000270
Sphere Wall (Eqs.63, 64)	Surface	∞	166.3599
Location a (Eqs.66, 67)	'Effective' Surface	0.1354	0.2021

It can be seen from the first row of Table III that the values of Da_I and Da_{II} at *Location a* are very low. This indicates that gas-phase reactions at the location of breakdown occur on larger time scales compared to that of advection and diffusion.

The second row of Table III compares the advection and diffusion processes at the wall with the surface recombination rate. At the wall, advection vanishes due to the no-slip velocity boundary condition and the value of Da_I, which is a ratio of the advection time scale to the surface reaction time scale, tends to ∞. However, the value of Da_{II} – ratio of the diffusion time scale to the surface reaction time scales at the wall – is $\mathcal{O}(2)$, indicating that diffusion is mainly responsible for the transport of O towards the wall for initiating surface recombinations. Thus, the molecular flux emerging from the wall is dependent on the rate at which diffusion transports atomic species towards the sphere surface. This diffusion – surface chemistry coupling is responsible for the steep decrease in atomic O that is observed close to the sphere wall (Fig. 5).

The Da_I and Da_{II} values in the third row of Table III indicate that at *Location a*, both advection and diffusion processes occur on time scales comparable to those of the 'effective' surface recombinations. Thus, the near wall region is characterized by chemical non-equilibrium, and the GCE diffusion flux breakdown parameter captures the continuum breakdown resulting from these competing mechanisms.

The GCE diffusion breakdown parameter represents a ratio of the diffusion velocity to the most probable speed of the gas. For the case under study, diffusion and thermal motion of the gas occur on comparable speeds and hence, the diffusion breakdown parameter exceeds the breakdown threshold of 0.05 (Fig. 3 (a)). Thus, chemical reactions set up steep concentration gradients giving rise to diffusion fluxes, which in this case are strong enough to distort the equilibrium Maxwellian of the VDF leading to continuum breakdown.

The above analysis indicates that the Damköhler numbers, by comparing the flow and diffusion time scales with the reaction time scale provide an estimate of the extent of chemical non-equilibrium for the system. It is found that continuum breakdown as indicated by the GCE species-wise diffusion breakdown parameter coincides with the regions of strong chemical non-equilibrium.

D. Comparison with the Kn_{GLL} Breakdown Parameters

Figs. 6 and 7 show the GCE and GLL breakdown parameters plotted against wall normal distance along the two extreme angular positions, namely $\theta = 0°$ and $90°$. The $\mathrm{Kn_{GLL}}$ has been evaluated for translational and vibrational temperature, velocity magnitude and individual species density based on Eq. 2. The chemically reacting nature of the flow causes species concentrations to fall to very low values at certain locations in the flow field, leading to mathematical anomalies in the computation of the species-wise $\mathrm{Kn_{GLL}}$. To overcome this, the Q_{local} in Eqn. 2 is set to $max(\rho_s, 0.001 * \rho_{total})$ where ρ_{total} is the total density at the location under consideration, similar to procedure employed in the computation of the $D^s_{GCE,i}$.
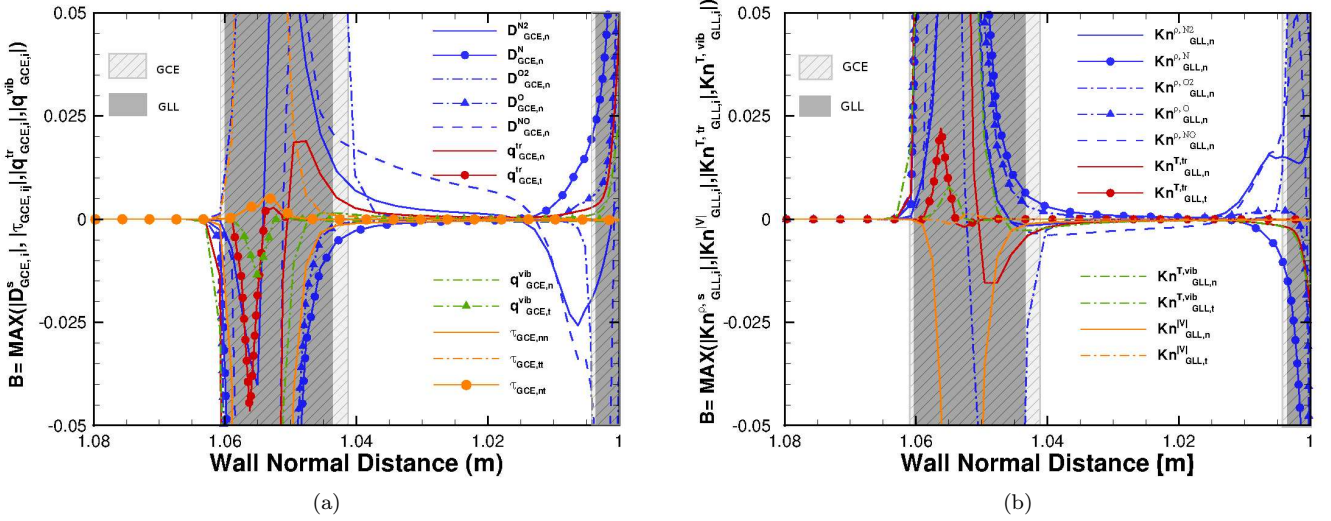

FIG. 6. Comparison of GCE and GLL breakdown parameters along stagnation line $\theta = 0°$: (a) GCE Breakdown Parameters (b) GLL Breakdown Parameters. The hatched areas represent the breakdown region indicated by the GCE parameters whereas, the solid gray fill indicates the breakdown region predicted by the GLL formulation.

The GLL breakdown regions are indicated by solid gray fill and the GCE breakdown regions are denoted by the hatched lines, for all continuum breakdown zones. The breakdown regions indicate that atleast one of the breakdown parameters have exceeded a threshold value of $B = 0.05$. Thus, these shaded areas represent regions in the flow field where continuum approximation fails to describe the flow system, and a kinetic-based solution methodology needs to be applied.

Figs. 6 show the GCE and GLL breakdown regions, along $\theta = 0°$. Both GCE and GLL breakdown parameters predict the onset of continuum breakdown approaching the shock due to large translational temperature gradients ($q^{tr}_{GCE,n}$ and $\mathrm{Kn^{tr}_{GLL,n}}$) at nearly identical locations along the stagnation line, $\theta = 0°$ (Figs. 6(a), 6(b)). The differences in the prediction of continuum breakdown in approaching the shock becomes apparent for increasing angle θ, and is prominent at the $\theta = 90°$ orientation (Fig. 7). It is observed that the GLL formulation predicts the 'start-of-shock' breakdown location downstream of that indicated by the GCE breakdown parameters (Figs. 7(a), 7(b)). This shift in the 'start-of-shock' location arises due to the difference in the coefficients of ∇T in the $q^{tr}_{GCE,n}$ and $\mathrm{Kn^{tr}_{GLL,n}}$ parameters. As outlined in Section III E, the ratio of $q^{tr}_{GCE,n}$ to $\mathrm{Kn^{tr}_{GLL,n}}$ for a single species system is $15\sqrt{\pi}/16$. For the 11-species air mixture considered in this study, this ratio was found to be around 2. As θ increases, the shock strength (and the corresponding temperature gradient) decreases, and the disparity between $q^{tr}_{GCE,n}$ and $\mathrm{Kn^{tr}_{GLL,n}}$ in predicting the onset of breakdown in the shock region is amplified.

It is observed that $\mathrm{Kn^{\rho,O_2}_{GLL,n}}$ predicts start of the near wall breakdown region slightly downstream of that indicated by the GCE parameter in Figs. 6 and 7. Similarly, along the $\theta = 90°$ position, the GCE diffusion parameter predicts a larger 'post-shock' breakdown region than the corresponding GLL terms. The GCE formulation considers a non-dimensionalized form of the species-wise diffusion fluxes to determine continuum breakdown, rather than accounting
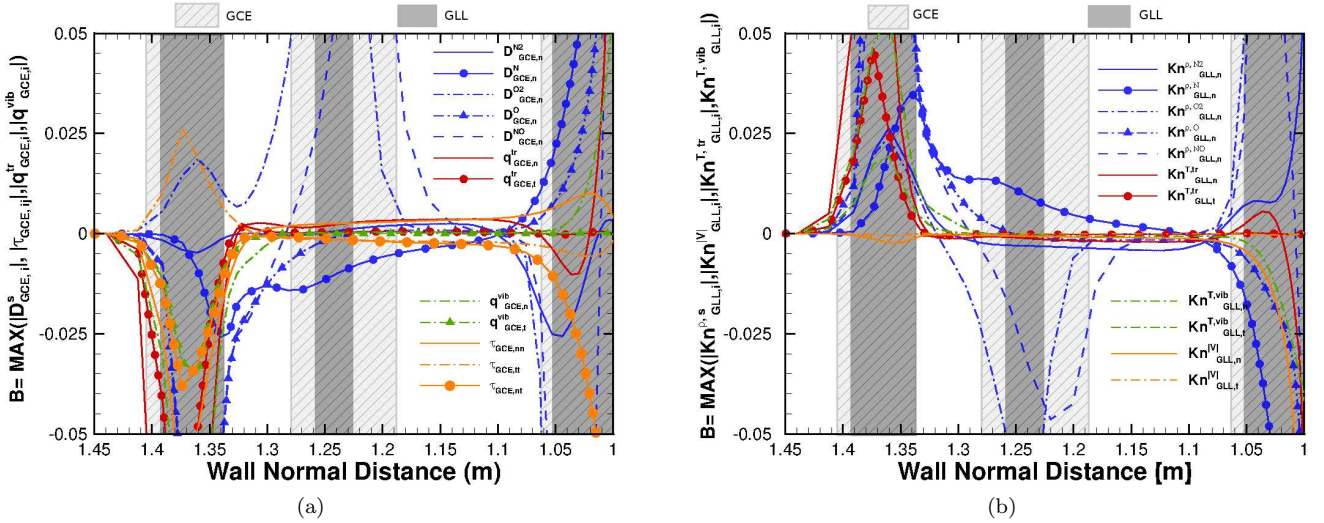
FIG. 7. Comparison of GCE and GLL breakdown parameters along $\theta = 90°$: (a) GCE Breakdown Parameters (b) GLL Breakdown Parameters. The hatched areas represent the breakdown region indicated by the GCE parameters whereas, the solid gray fill indicates the breakdown region predicted by the GLL formulation.

for only the species-wise density gradients. Further, the representation of diffusion breakdown in the GCE framework considers the contribution of the species number density gradient and pressure gradients to the diffusion driving force – which are responsible for diffusion fluxes (Eq. 19). The contribution of this pressure gradient term to the diffusion driving force (Eq. 19), in turn depends on the abundance and the mass density of the species under consideration relative to the mixture. Also, the effect of the species-wise diffusion coefficients are also taken into account by the GCE formulation, but the GLL density gradient parameter does not incorporate this feature. These differences in the breakdown parameter definitions are the likely reasons for the disparity in the results observed between the GCE and GLL formulation with regards to species-wise diffusion breakdown.

V. CONCLUSIONS

The Generalized Chapman-Enskog method for rapid and slow processes was used to develop a robust set of continuum breakdown parameters for chemically reacting flows from kinetic theory. These continuum breakdown parameters are derived for one-temperature, two-temperature and three-temperature models and may readily be applied to analyze continuum breakdown from a CFD flow field solution. The full set of GCE continuum breakdown parameters includes breakdown mechanisms predicted by diffusion processes (multi-component and thermal), normal and shear stresses, Fourier-type heat fluxes based on translation, rotational and vibrational temperatures, bulk viscosity, and relaxation pressure. These GCE breakdown parameters, derived from rigorous kinetic theory, are able to accurately capture the proper mechanism leading to the breakdown of all the transport processes, unlike the existing phenomenological breakdown parameters.

The GCE parameters were then used to analyze continuum breakdown for a Mach 24 reacting flow over a sphere. Continuum breakdown was observed due to the strong translational, vibrational heat fluxes at the shock location. Along the stagnation line, the strong species diffusion fluxes due to dissociation/recombination reactions at the shock were also found to perturb the system's VDF. The species-wise diffusion breakdown parameter was instrumental in determining the 'end-of-shock' breakdown location. Diffusion-driven processes resulting from gas-phase and surface chemical reactions were also found to play an important role in determining the location of the near wall breakdown region. Thus, chemical reactions which are a major source for setting up species concentration gradients, can indirectly distort the VDF by means of strong diffusion fluxes leading to continuum breakdown.

It is also noted that thermal and velocity-slip models have often been employed in CFD calculations to account for non-continuum effects near a solid surface. While such slip models may be well-suited for continuum breakdown in simple gas flows where breakdown due to large velocity gradients (i.e., normal and shear stresses) or temperature gradients (i.e., heat fluxes) dominate, the breakdown occurring due to species-wise diffusion fluxes, are not likely to be captured by a slip model.

VI. ACKNOWLEDGMENTS

[1] GA Bird, *The DSMC method* (CreateSpace Independent Publishing Platform, 2013).
[2] Roberto Roveda, David B Goldstein, and Philip L Varghese, "Hybrid euler/particle approach for continuum/rarefied flows," J. Spacecraft Rockets **35**, 258–265 (1998).
[3] Jonathan M Burt and Iain D Boyd, "A hybrid particle approach for continuum and rarefied flow simulation," J. Comp. Phys. **228**, 460–475 (2009).
[4] Thomas E Schwartzentruber and Iain D Boyd, "A hybrid particle-continuum method applied to shock waves," J. Comp. Phys. **215**, 402–416 (2006).
[5] Thomas E Schwartzentruber, Leonardo C Scalabrin, and Iain D Boyd, "A modular particle–continuum numerical method for hypersonic non-equilibrium gas flows," J. Comp. Phys. **225**, 1159–1174 (2007).
[6] V. I. Kolobov, R. R. Arslanbekov, V. V. Aristov, A. A. Frolova, and S. A. Zabelok, "Unified solver for rarefied and continuum flows with adaptive mesh and algorithm refinement," J. Comp. Phys. **223**, 589–608 (2007).
[7] S. Chapman and T. G. Cowling, *The mathematical theory of non-uniform gases* (Cambridge university press, 1970).
[8] G A Bird, "Breakdown of Translational and Rotational Equilibrium in Gaseous Expansions," AIAA Journal **8**, 1998–2003 (1998).
[9] Iain D. Boyd, Gang Chen, and Graham V. Candler, "Predicting failure of the continuum fluid equations in transitional hypersonic flows," Physics of Fluids **7**, 210 (1995).
[10] S Chigullapalli, A Venkattramana, M S Ivanov, and A A Alexeenko, "Entropy considerations in numerical simulations of non-equilibrium rarefied flows," Journal of Computational Physics, Vol. 229, Issue 6 (2010).
[11] Timothy R Deschenes, Timothy D Holman, and Iain D Boyd, "Effects of Rotational Energy Relaxation in a Modular Particle-Continuum Method," Journal of Thermophysics and Heat Transfer **25** (2011).
[12] Timothy R. Deschenes and Iain Boyd, "Extension of a Modular Particle-Continuum Method to Vibrationally Excited, Hypersonic Flows," AIAA Journal **49**, 1951–1959 (2011).
[13] A Garcia and B Alder, "Generation of the Chapman-Enskog Distribution," J. Comp. Phys. **140**, 66–70 (1998).
[14] G.A Bird, *Molecular gas dynamics and the Direct Simulaton of Gas Flows* (Clarendon Press, Oxford, 1994).
[15] Wen Lan Wang and Iain D. Boyd, "Predicting continuum breakdown in hypersonic viscous flows," Physics of Fluids **15**, 91–100 (2003).
[16] Thomas E Schwartzentruber, Leonardo C Scalabrin, and Iain D Boyd, "Hybrid Particle Continuum Simulations of Nonequilibrium Hypersonic Blunt-Body Flowfields," Journal of Thermophysics and Heat Transfer **22** (2008).
[17] J. H. Ferziger and H. G. Kaper, *Mathematical theory of transport processes in gases* (North Holland, 1972).
[18] E. Nagnibeda and E. Kustova, *Non-equilibrium reacting gas flows: kinetic theory of transport and relaxation processes* (Springer Science & Business Media, 2009).
[19] K. A. Stephani, D. B. Goldstein, and P. L. Varghese, "A non-equilibrium surface reservoir approach for hybrid DSMC/Navier-Stokes particle generation," Journal of Computational Physics **232**, 468–481 (2013).
[20] P Gnoffo, "Application of program LAURA to three-dimensional AOTV flowfields," in *24th Aerospace Sciences Meeting* (Reno, Nevada, 1986) pp. 0–12.
[21] Peter A. Gnoffo, Ronald S. McCandless, and H. C. Yee, "Enhancements to Program LAURA for computation of three-dimensional hypersonic flow," in *25th AIAA Aerospace Sciences Meeting* (Reno, Nevada, 1987).
[22] J. D. Ramshaw, "Self-consistent effective binary diffusion in multicomponent gas mixtures," Journal of Non-Equilibrium Thermodynamics **15**, 295–300 (1990).
[23] J D Ramshaw and C H Chang, "Multicomponent diffusion in two-temperature magnetohydrodynamics," Physical Review E **53**, 6382–6388 (1996).
[24] Roop N. Gupta, Richard A. Yos, Jerrold M. Thompson, and Kam-Pui Lee, *A review of reaction rates and thermodynamic and transport properties for the 11-species air model for chemical and thermal nonequilibrium calculations to 30000 K*, Tech. Rep. (NASA-RP-1232, 1990).
[25] Raymond Brun, *Introduction to reactive gas dynamics* (OUP Oxford, 2009).
[26] J. Thoemel, O. Chazot, and P. Barbante, "Aspects of advanced catalysis modeling for hypersonic flows," in *Proceedings of the 2008 CTR Summer Program*, Center for Turbulence Research, Stanford University, Stanford, CA (2008) p. 29.